Effects of Freestream Turbulence, Turbulence Length Scale, and Reynolds Number on Turbine Blade Heat Transfer in a Transonic Cascade

Jeffrey S. Carullo

Thesis submitted to the faculty of the
Virginia Polytechnic Institute and State University
in partial fulfillment of the requirements for the degree of

Masters of Science
in
Mechanical Engineering

Dr. Wing Ng, Co-Chair
Dr. Karen Thole, Co-Chair
Dr. Clinton Dancey

December 11, 2006
Blacksburg, Virginia

Keywords: Freestream Turbulence, Turbulence Length Scale,
Turbine Blade, Heat Transfer, Cascade

Effects of Freestream Turbulence, Turbulence Length Scale, and Reynolds Number on Turbine Blade Heat Transfer in a Transonic Cascade

Jeffrey S. Carullo
Virginia Polytechnic Institute and State University, 2006
Advisors: Dr. Wing F. Ng and Dr. Karen A. Thole

Thesis Abstract

It is important to be able to accurately predict the heat transfer distribution over the component when designing components in the turbine section. The gas temperature exiting the combustor in many gas turbine engines has increased to be above the melting temperature of turbine components. These high gas temperatures can quickly degrade components and cause components to fail. To extend the life of components in the high gas temperature flows, cooling schemes are implemented on components. The cooling scheme designs are based upon heat transfer predictions in the design phase. Accurate predictions of the heat transfer distributions are important to properly apply cooling schemes. The component designers typically use computational fluid dynamics (CFD) or simple experiments in the design phase.

CFD is becoming more frequently used than experimentation in the design phase. Since CFD is heavily relied upon, accurate models are required. While the CFD has been proven to accurately predict the aerodynamic flow physics of turbine blades and vanes, the heat transfer predictions are still in need of some refinement. At high turbulence levels, most CFD programs significantly over predict the heat transfer levels. The purpose of this study is to investigate the effect of high freestream turbulence on heat transfer on gas turbine blades. This study will also provide the CFD modelers with heat transfer data at flow conditions that are representative of flow in gas turbine engine. This data can be used to improve their empirical correlations for use in their codes.

In this study, a turbine blade of geometry typical of a first stage turbine blade was tested in the Virginia Tech linear transonic cascade wind tunnel. Aerodynamic and heat transfer measurements were made on the turbine blade. The flow entering the blade cascade was also characterized by measuring the turbulence intensity, turbulence length scale and velocity uniformity. Measurements were made at exit Mach numbers of 0.55, 0.78 and 1.03 and

turbulence levels of 2%, 12% and 14% for each exit Mach number. The high turbulence levels were generated using passive turbulence grids.

Effects of Freestream Turbulence, Turbulence Length Scale, and Reynolds Number on Turbine Blade Heat Transfer in a Transonic Cascade

Preface

The combustion temperature of gas turbine engines continue to increase in order to get a higher work output and higher efficiency from gas turbine engines. To handle the high temperature gas, turbine designers have developed cooling schemes that can keep turbine components from degrading from the exposure to the hot gases. Typically, turbine designers utilize computational fluid dynamics (CFD) to predict the regions of components that will require a cooling scheme to be implemented. While the CFD has been proven to accurately predict the flow fields, the heat transfer predictions still need some refinement. At high turbulence levels that are typical of the flow exiting the combustor, heat transfer predictions tend to be significantly higher than experimental values. This study examines the effect of freestream turbulence and the turbulence length scale on the heat transfer distribution on a turbine blade. The data from this experiment can be used to refine heat transfer models.

This thesis consists of two sections. The first section is a paper that was submitted to the 2007 International Gas Turbine Institute (IGTI) Conference. The paper reports on the effects of freestream turbulence and turbulence length scale on the heat transfer distribution on a turbine blade. The second section of this thesis consists of appendices that support the IGTI paper. It includes additional details about the data collection and reduction procedures on the pressure distributions and turbulence measurements that were made on the turbine blade.

Acknowledgments

This work was supported by Solar Turbines and monitored by Dr. Hee-Koo Moon and Dr. Luzeng Zhang. I would like to thank Dr. Moon and Dr. Zhang for their guidance on this project and for their mentoring while I was working at Solar Turbines.

I would like to express my gratitude to the members of my committee for all of their help. Dr. Ng has guided me through all of the experiments performed in the transonic cascade wind tunnel. He has taught me the value of time management to become an effective worker. Dr. Thole has always been there for me no matter how busy she was. I want to thank her for convincing me to stay for graduate school and all of her insight to turbine blade heat transfer. I also appreciate her help in revising my papers and presentations. Dr. Dancey has always been such a great professor and his compressible flow course was the reason that I became interested in turbomachinery.

Thank you to Bill Songer, Johnny Cox, James Dowdy, and Tim Kessinger in the Mechanical Engineering Machine Shop for all of their help. This project would not have been possible without all of their hours of machine work and all of their help. Bill your help was invaluable and I learned even more about machining from you. A thank you also goes out to Steve Edwards for his assistance in teaching us how to run the wind tunnel facility and supporting us throughout our project.

The support of my friends and peers has been invaluable. It was through the support of my research partners Shakeel Nasir, Ashley Guy and Ronnie Cress that I was able to successfully complete my research. We stuck together to get through this project and were successful. I learned a great deal from you guys and to that I am grateful. To my officemates, Jonathan and Hugh for keeping me sane through all those hours spent in 210B. Steve, Joe, Seth and the rest of the VTExCCL guys for their help. I could always count on you guys to have the tools that I needed to borrow. Mike, thank you for the help in keeping me focused for all of those hours of hard work to get through Dr. Vick's classes. Your friendship helped to get me through graduate

school. Patrick, thank you for being such a great friend and colleague. You were always there for me through the tough times and I could always count on you. We all miss you buddy.

Finally, I would like to thank my family for all of their love and support. Mom, Dad and Keri, thank you for being there for me and for your support. Lindsay are the one who made this all possible. If it was not for your love and support I never would have made it through graduate school.

Table of Contents

List of Tables

List of Figures

The Effects of Freestream Turbulence, Turbulence Length Scale, and Exit Reynolds Number on Turbine Blade Heat Transfer in a Transonic Cascade

J.S. Carullo, S. Nasir, R.D. Cress, W.F. Ng and K.A. Thole
Mechanical Engineering Department
Virginia Polytechnic Institute and State University
Blacksburg, VA 24061

L.J. Zhang and H.K. Moon
Solar Turbines Inc.
San Diego, CA 92101

Submitted to the 2007 IGTI Conference

Abstract

This paper experimentally investigates the effect of high freestream turbulence intensity, turbulence length scale, and exit Reynolds number on the surface heat transfer distribution of a turbine blade at realistic engine Mach numbers. Passive turbulence grids were used to generate freestream turbulence levels of 2%, 12%, and 14% at the cascade inlet. The turbulence grids produced length scales normalized by the blade pitch of 0.02, 0.26, and 0.41, respectively. Surface heat transfer measurements were made at the midspan of the blade using thin film gauges. Experiments were performed at exit Mach numbers of 0.55, 0.78 and 1.03 which represent flow conditions below, near, and above nominal conditions. The exit Mach numbers tested correspond to exit Reynolds numbers of 6×10^5, 8×10^5, and 11×10^5, based upon true chord.

The experimental results showed that the high freestream turbulence augmented the heat transfer on both the pressure and suction sides of the blade as compared to the low freestream turbulence case. At nominal conditions, exit Mach 0.78, average heat transfer augmentations of 23% and 35% were observed on the pressure side and suction side of the blade, respectively.

Nomenclature

C	true chord of blade
C_p	constant pressure specific heat
d	leading edge diameter of blade
Fr	Frossling number
h	heat transfer coefficient
k_a	thermal conductivity of air
k	acceleration parameter
Ma	Mach number
Nu	Nusselt number
Nu_0	Nusselt number at Tu = 2%
P	pitch of blade
Pr	Prandtl number
q”	heat flux
r_c	recovery factor
Re	Reynolds number
s	surface distance on from stagnation point
St	Stanton number
T	temperature
Tu	freestream turbulence in streamwise direction
U	local velocity
VR	velocity ratio

Greek

γ	specific heat ratio of air
Λ_x	integral turbulence length scale (LS)
ρ	local density of air

Subscripts

aw	adiabatic wall
in	inlet conditions
o	stagnation

Introduction

The components in the turbine section of a gas turbine engine present several complex problems to engine designers. One of the problems that designers face is the high gas path temperatures that pass through the turbine section. The gas path temperatures continue to be increased in order to increase the gas turbine power output and efficiency. In most engines, the gas path temperature has increased to be well above the melting temperature of most engine components. These high temperatures can drastically decrease the operating life of an engine component if not cooled properly.

Designers typically use CFD and other analysis tools to predict the regions of a component that will require a cooling scheme to be used. When modeling the flow through a blade passage, a designer has a variety of turbulence models to choose from. These turbulence models are based on physical laws as well as empirical data. The efforts of this work are to provide the model developers with experimental data collected at realistic engine Mach number conditions.

Summary of Past Literature

The freestream turbulence in the turbine section of an engine is due to the velocity fluctuations of the flow created by the combustor system and vane wakes upstream of the blade passages. While measuring the turbulence level in a gas turbine is extremely difficult, researchers have found that combustion systems typically produce turbulence levels between 7% and 30% [1.1-1.2]. The turbulence produced by the combustor decays as the flow passes through the vanes, but additional velocity fluctuations will be created by the vane wakes.

Several experimental studies have been performed in transonic cascades that investigate the effects of exit Reynolds number and freestream turbulence on the surface heat transfer distribution over a turbine blade. Consigny and Richards [1.3] measured the blade surface heat transfer distribution by varying the freestream turbulence between 0.8% and 5.2%. Consigny and Richards observed that increasing the turbulence level augmented the heat transfer on the pressure and suction sides and at the leading edge. An earlier transition to a turbulent boundary layer was observed on the suction side of the blade when the turbulence level was increased.

Another study by Arts et al. [1.4] examined the effect of Mach number, Reynolds number and incidence angle while varying the turbulence levels between 1% and 6%. Similarly to Consigny and Richards, Arts et al. observed an earlier boundary layer transition on the suction side when the freestream turbulence level increased. In addition, Arts et al. noted a local peak in heat transfer on the pressure side near the leading edge. The local peak amplitude diminished as the turbulence level increased. The location of the local peak corresponds to a deceleration of the flow downstream of the leading edge on the pressure surface. They hypothesized that a small recirculation bubble occurred in the decelerating region and caused the local peak in heat transfer. Arts et al. also observed that increasing the exit Reynolds number increased the heat transfer levels.

More recent studies by Giel et al. [1.5] examined the effects of Reynolds number and cascade end wall boundary layers on surface heat transfer at turbulence levels of 9% with an integral lengths scale of 26 mm (1.02 in.). Giel et al. also observed a local peak on the pressure side of the blade near the leading edge. From these experiments and other similar experiments, turbulence models have been created and validated.

Experimental Setup and Instrumentation

Wind Tunnel Facility

The two-dimensional transonic cascade wind tunnel, shown in Figure 1.1, is a blow-down facility that is capable of sustaining a constant test section pressure for up to 25 seconds. Air is supplied from high pressure air tanks that are charged up to 1380 kPa (200 psig) prior to testing. A control valve regulates the flow from the air tanks to the test section. Cascade inlet pressures range from 20.7 kPa (3 psig) to 69.0 kPa (10 psig) depending on the objective test conditions. Between the control valve and the test section, the air passes through a passive heat exchanger, which heats the cascade inlet flow up to 120°C. After the air passes through the heat exchanger, the air goes through a contraction and enters the test section before being exhausted to the atmosphere. Because of facility constraints, an increase in the exit Mach number is coupled to an increase in the exit Reynolds number.

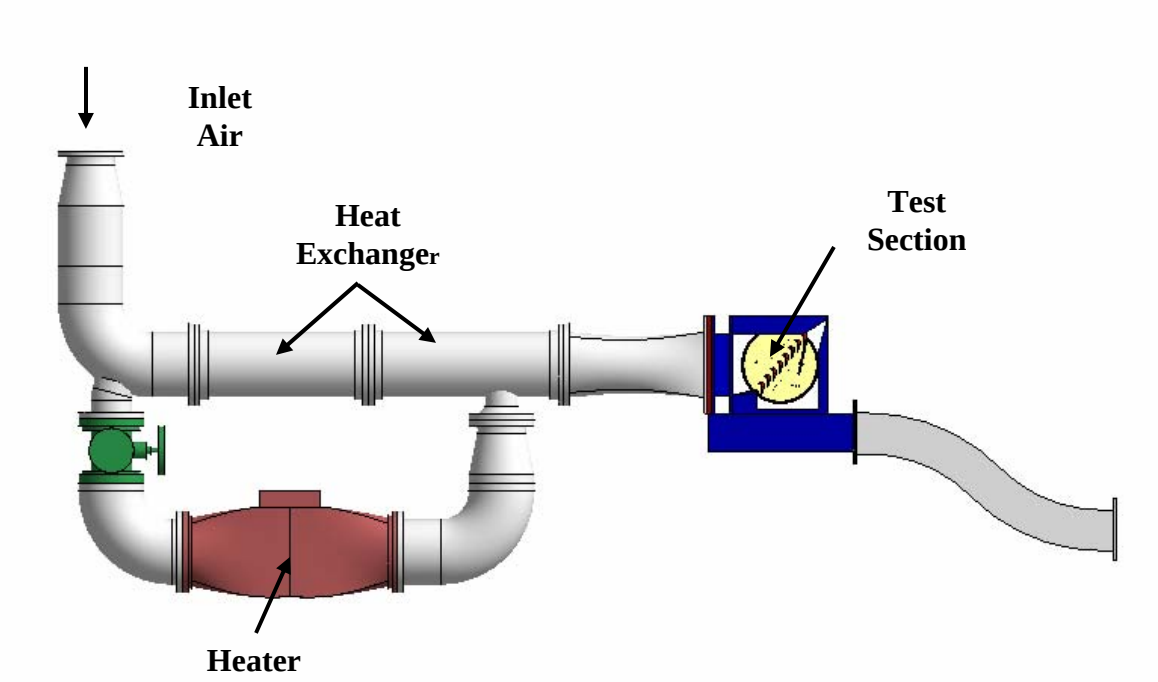

Figure 1.1. Transonic cascade wind tunnel

The turbine blade tested in these experiments is similar in geometry to a first stage turbine blade. The blade was scaled two times so that the nominal exit Reynolds number would be at the desired value. Table 1.1 summarizes the geometry of the turbine blade.

Table 1.1. Turbine blade geometry

True Chord	69.9 mm (2.75 in.)
Axial Chord	35.2 mm (1.39 in.)
Pitch	58.2 mm (2.29 in.)
Span	152.4 mm (6.00 in.)
Turning Angle	107.5°

A diagram of the blade cascade is provided in Figure 1.2. From the blade geometry and the test section size, the blade cascade consists of seven full blades and two partial blades, which result in seven full passages and one partial passage. A tailboard placed at the blade exit angle aids in creating periodic flow through the cascade. The blades are numbered starting from the lower left of the cascade with blade 4 being the blade that is fully instrumented to make static pressure and heat transfer measurements. The slot located upstream of the cascade is used to measure the turbulence and velocity distributions at the inlet of the cascade.

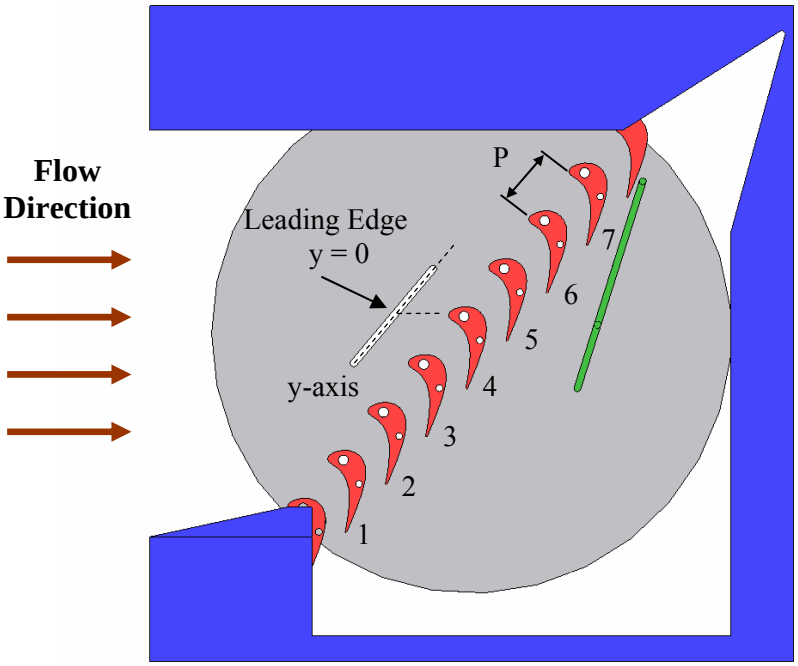

Figure 1.2. Cascade diagram showing the blades and the axis orientation for measurements with the traverse

Static Pressure Measurements

To calculate the isentropic Mach number distribution on the blade surface, the turbine blade was instrumented with static pressure taps placed at the midspan of the blade. Blade 4 was instrumented with a total of 27 pressure taps with 9 taps on the pressure side, 17 taps on the suction side and 1 tap near the leading edge. Static pressure taps were also instrumented on suction side of blade 3 and on the pressure side of blade 5 to check the periodicity of the flow. The static pressure measurements were made through independently conducted experiments relative to the heat transfer experiments. In addition to calculating the isentropic Mach number distribution, the acceleration parameter distribution on the blade surface was also calculated.

Heat Transfer Measurements

Heat transfer measurements were made with thin film gauges. Thin film gauges were originally developed by Schultz and Jones [1.6] and variations of the original design have been used by Doorly and Oldfield [1.7] and Dunn [1.8]. The thin film gauges that were used in these experiments were manufactured according to procedure described by Joe [1.9]. A photograph of the gauges installed on the blade is shown in Figure 1.3. Thin film gauges allow for high spatial resolution measurements on the blade surface. Each thin film gauge consists of a platinum wire

that is 3.18 mm (0.125 in.) long and copper leads that are sputtered to a Kapton sheet. The Kapton sheet with the gauges is attached to a blade manufactured from a low thermal conductivity ceramic material called Macor. The platinum wire is the sensing area of the gauge and was placed at the midspan of the blade. A total of 36 thin film gauges were instrumented on the blade.

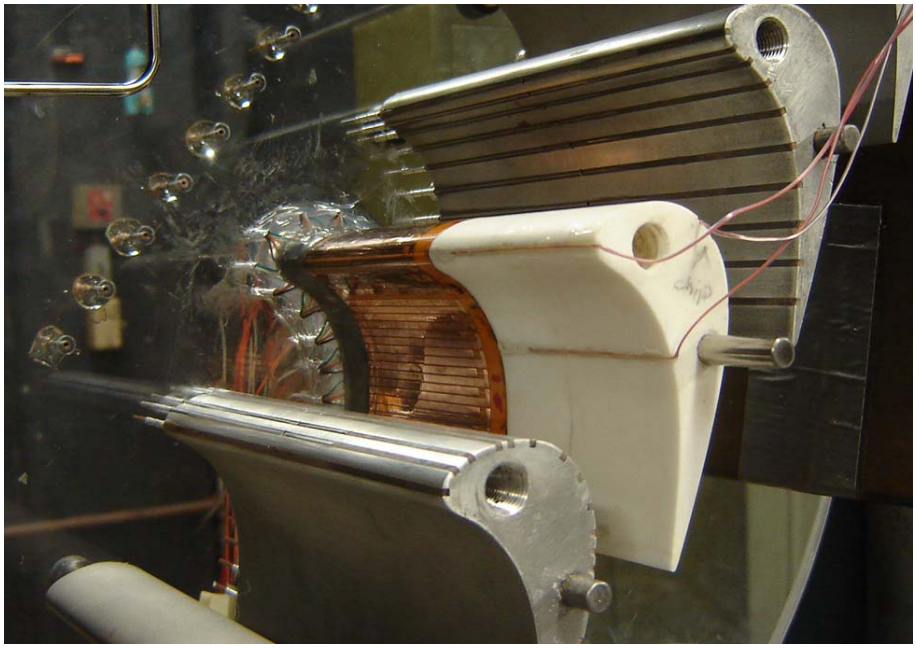

Figure 1.3. Picture of thin film gauges in wind tunnel

The thin film gauge operates by changing resistance with temperature. A calibration of each gauge was performed prior to testing. Since the gauge changes resistance with temperature, the gauge is used as one arm of a Wheatstone bridge circuit and the change in voltage output of the bridge is recorded during the experiment. The data from up to 31 gauges can be recorded in this facility during a single test.

To reduce the heat transfer data, several steps must be taken. The voltage output from each Wheatstone bridge is converted into surface temperature using the calibration curve and basic Wheatstone bridge operating principles. Next, the heat flux for each gauge is calculated by using a finite-difference code developed by Cress [1.10] that solves the one-dimensional, transient heat conduction equation. The heat transfer coefficient can then be calculated by using,

$$h = \frac{q''}{(T_{aw} - T_{gauge})} \tag{1.1}$$

The adiabatic wall temperature is provided by,

$$T_{aw} = T_o \cdot \left(\frac{1 + r_c \cdot \frac{\gamma - 1}{2} Ma^2}{1 + \frac{\gamma - 1}{2} Ma^2} \right) \tag{1.2}$$

It was assumed that the boundary layer was turbulent everywhere, so a recovery factor of $r_c = Pr^{1/3}$ was applied to all of the gauges. The heat transfer coefficient can then be nondimensionalized by calculating the Nusselt number by using,

$$Nu = \frac{h \cdot C}{k_a} \tag{1.3}$$

The heat transfer coefficient can also be nondimensionalized in terms of the Stanton number given by,

$$St = \frac{h}{\rho \cdot U \cdot C_p} \tag{1.4}$$

Uncertainty Analysis

The experimental uncertainty of the heat transfer measurements was calculated by using the procedure developed by Moffat [1.11]. The analysis took into account the bias error and precision error. An uncertainty was calculated for each gauge at every test condition. The total uncertainty of the heat transfer coefficient for the gauges ranged between 8.5% and 11.5% with the bias error contributing the majority to the total uncertainty.

Turbulence Generation

To generate freestream turbulence levels of 12% and 14%, passive turbulence grids were used. A schematic of the turbulence grids is provided in Figure 1.4. The grid designs were based on the correlations reported by Baines and Peterson [1.12] and research performed by Nix et al. [1.13] on turbulence grids in the cascade wind tunnel. The first turbulence grid is a square mesh grid. The square mesh grid has bar widths of 1.91 cm (0.75 in.) and spaced to create 3.81cm x 3.81cm (1.5 in. x 1.5 in.) square openings. The solidity of the square mesh grid is 48%. The second turbulence grid is a parallel bar grid. This grid has bars that are 6.35cm (2.5 in.) wide and spaced 4.76 cm (1.875 in.) apart to create a solidity of 50%.

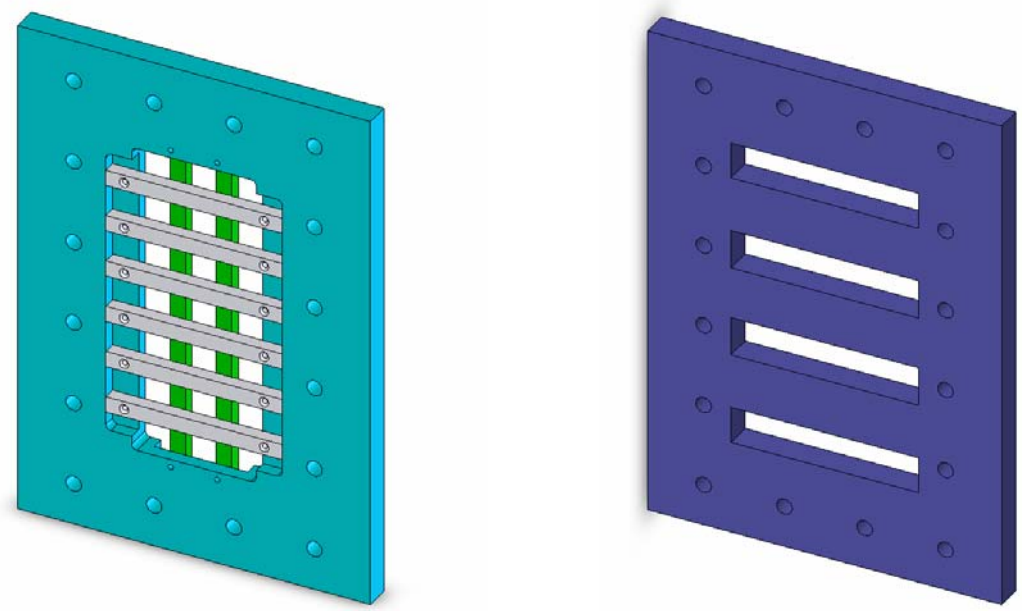

(a) (b)

Figure 1.4. Turbulence grids (a) mesh grid, Tu = 12% and (b) bar grid, Tu = 14%

The velocity fluctuations in the streamwise direction were measured using a single hot-wire probe. The hot-wire probe was discretely traversed over one blade pitch along the slot parallel to the blade inlet plane. The slot is located 0.6C upstream of the blades and shown in Figure 1.2. The turbulence intensity and integral turbulence length scales were calculated at each measurement location. Taylor's Hypothesis of frozen turbulence was applied to calculate the integral length scale. The turbulence levels and length scales were measured for the square mesh grid, the bar grid and a baseline case where no turbulence grid was installed in the tunnel. The turbulence intensity and integral length scale distributions along the blade inlet pitch is provided in Figures 1.5 and 1.6, respectively. The turbulence levels and normalized length scales are provided in Table 1.2.

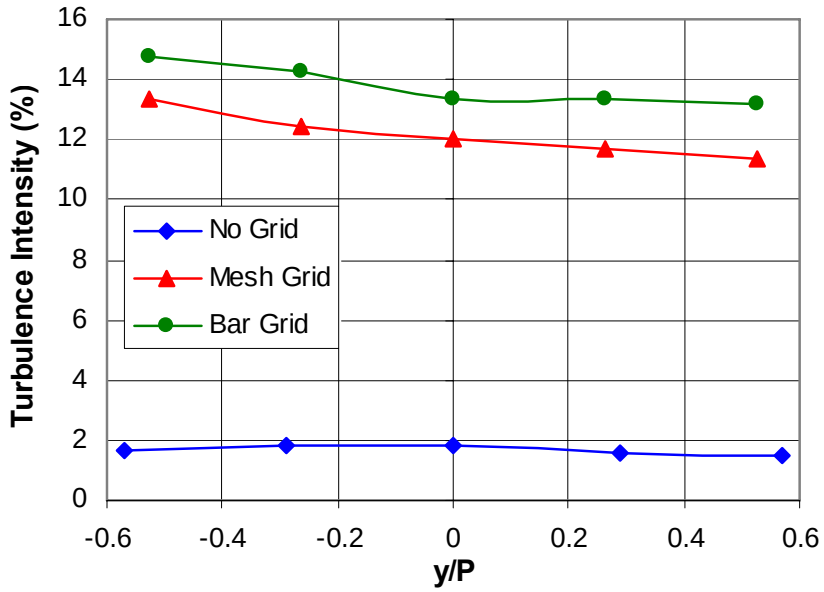

Figure 1.5. Turbulence intensity along inlet pitch

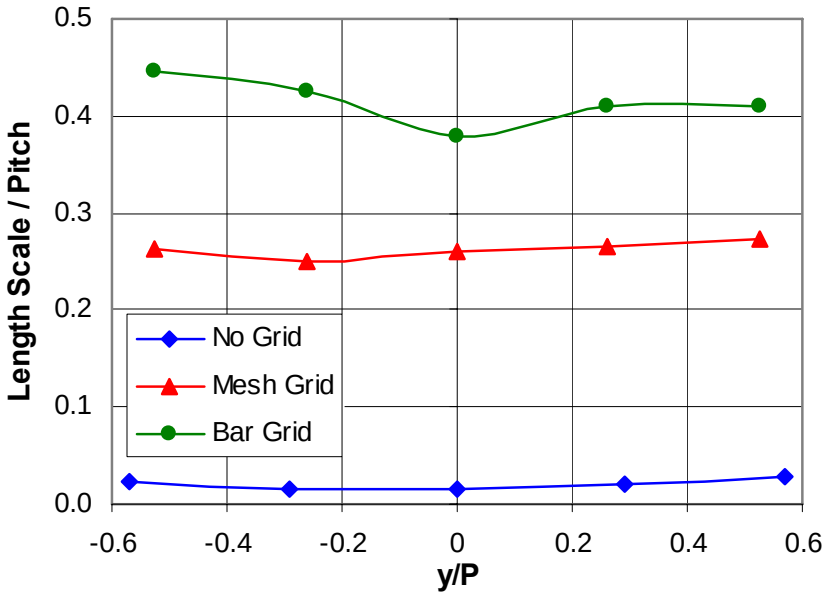

Figure 1.6. Integral length scale along inlet pitch

Table 1.2. Summary of grid generated turbulence

	Turbulence Intensity	Length Scale (Λ_x/P)
Baseline	2%	0.02
Mesh Grid	12%	0.26
Bar Grid	14%	0.41

To check that the inlet flow to the blade passages downstream of the turbulence grids was uniform, a Kiel probe was traversed along the angled slot. A ratio of the velocity from the Kiel probe to the velocity measured from a stationary Pitot probe was calculated. The velocity ratio for the each configuration tested is provided in Figure 1.7. The bar grid shows a slight variation of inlet velocity along the angled slot. The trade off of generating high turbulence levels with the bar grid was that the inlet velocity was slightly nonuniform.

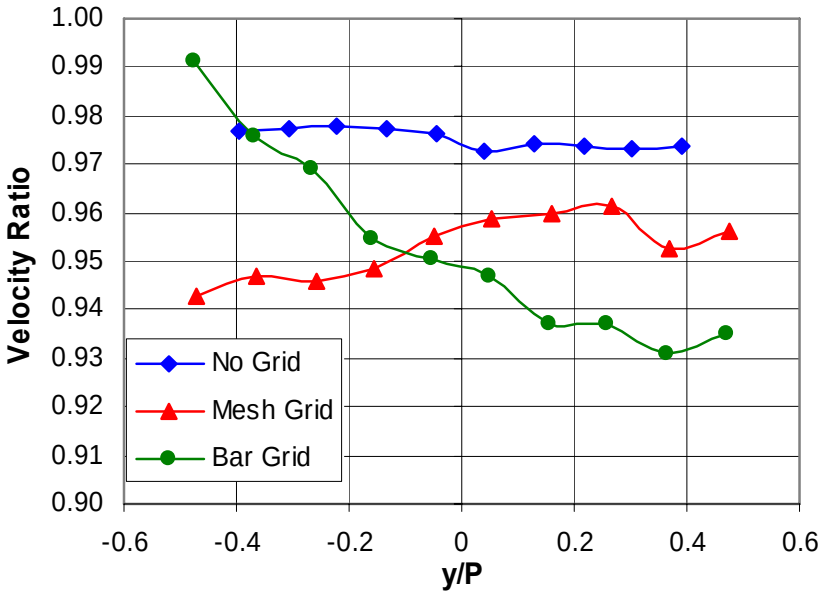

Figure 1.7. Velocity ratio distribution along inlet pitch

Blade Static Pressure Distribution

Figure 1.8 shows the local Mach number distributions on the blade surface for three exit Mach number conditions. The flow accelerates over most of the pressure side except for a short deceleration region just downstream of the stagnation point (s/C = -0.25). The flow on the suction side continuously accelerates up to the geometric throat area (s/C = 0.84). The exit Mach 0.6 and 0.85 cases decelerate immediately after the throat, whereas the exit Mach 1.1 case continues to accelerate and becomes supersonic before beginning to decelerate.

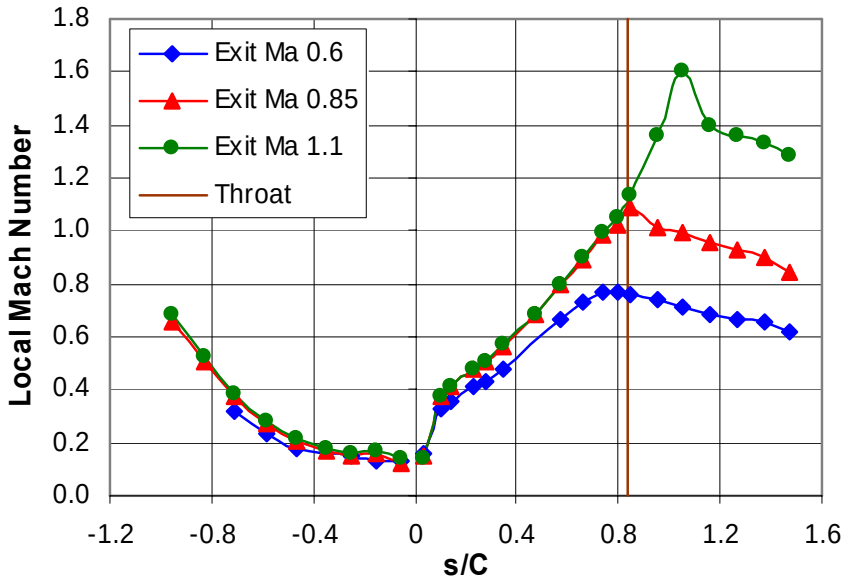

Figure 1.8. Local Mach number distribution over blade

The periodicity of the flow at exit Mach 0.85 is provided in Figure 1.9. The flow periodicity is shown by comparing the local Mach number distribution over the blade surfaces. The suction side of blade 3 and blade 4 shows the same local Mach number distributions over the majority of the suction surface. There is only a slight variation in the local Mach numbers near the geometric throat. The pressure side of blade 4 and blade 5 shows almost identical local Mach number distributions.

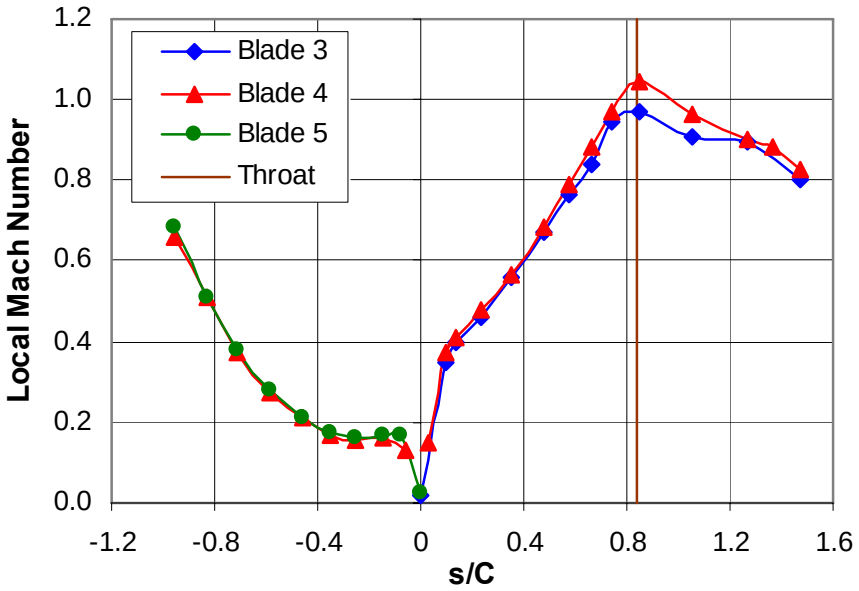

Figure 1.9. Flow periodicity through blade passages

The distribution of the acceleration parameter on the blade surface for each exit Mach number is provided in Figure 1.10. The acceleration parameter distribution shows the same trends as the local Mach number distribution. A positive acceleration parameter indicates that the flow is accelerating and a negative value indicates that the flow is decelerating. On the pressure side of the blade, the acceleration parameter is above the critical value of 3 x 10^{-6} which has been observed by Launder and Jones [1.14] and reported in the transition study by Mayle [1.15] to relaminarize the boundary layer.

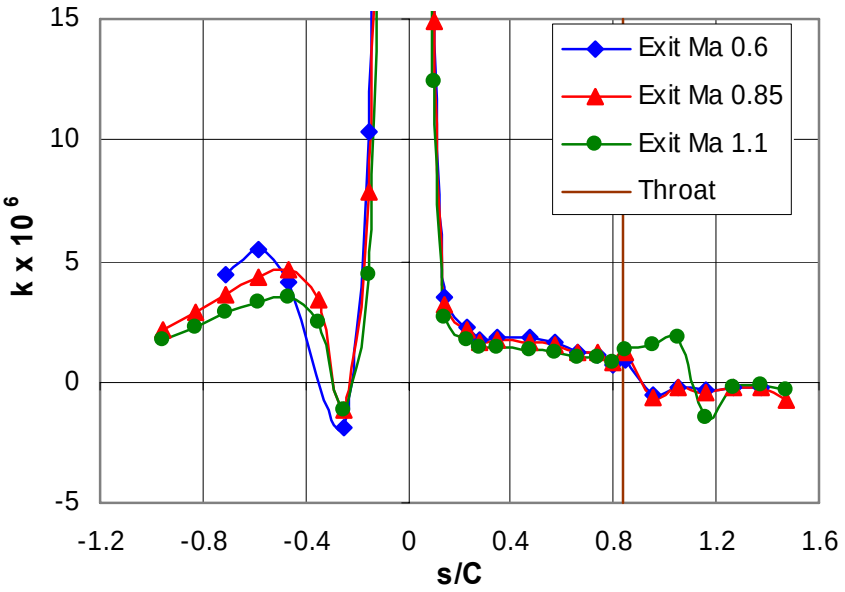

Figure 1.10. Distribution of the acceleration parameter over the blade

Blade Heat Transfer Distribution

Test Conditions

Heat transfer measurements were performed at exit Mach numbers of 0.55, 0.78, and 1.03. The turbulence levels were varied between 2%, 12%, and 14% at each exit Mach number. The test matrix resulted heat transfer data for nine different flow conditions. For each flow condition, measurements were performed at least three times to ensure that the data were repeatable. Table 1.3 provides the flow conditions for each test.

Table 1.3. Test conditions for each case

	Exit Ma	Tu	Exit Re
Case 1	0.57	2%	640,000
Case 2	0.55	12%	610,000
Case 3	0.55	14%	600,000
Case 4	0.76	2%	810,000
Case 5	0.78	12%	790,000
Case 6	0.78	14%	800,000
Case 7	1.03	2%	1,090,000
Case 8	1.03	12%	1,060,000
Case 9	1.01	14%	1,070,000

Effect of Freestream Turbulence

This section discusses the effect that increasing the freestream turbulence has on the heat transfer distribution over the turbine blade surface. Plots are shown of the heat transfer distribution over the blade surface in terms of Nusselt number and the Nusselt number augmentation relative to the low freestream turbulence cases. The data is also compared with the flat plate correlations for laminar and turbulent boundary layers. Each of these plots is presented for each exit Mach number condition tested.

Figure 1.11 provides the heat transfer distribution plot for each freestream turbulence level at exit Mach 0.55. The turbulence augments the heat transfer at the leading edge, on the pressure side and the suction side of the blade. On the suction side, the transition to a turbulent boundary layer occurs near the throat (s/C = 0.84) for each turbulence level. For the 2% turbulence case, the transition takes place downstream of the throat at s/C = 0.87. The boundary layer transition length over the blade surface is short because of the decelerating flow.

The 12% and 14% turbulence cases both show transition occurring just upstream of the throat (s/C = 0.72). The transition length has increased for the high turbulence cases because the flow is still accelerating up to the throat. The length of the boundary layer transition increases when the flow is accelerating. The effect of acceleration on the transition length was also noted in the study performed by Zhang and Han [1.16]. Once the boundary layer goes turbulent, the effect of the freestream turbulence level on heat transfer diminishes. Both turbulence levels tested show very similar trends in augmenting the turbulence even though the length scales are different.

The heat transfer data at the high turbulence levels are normalized with the 2% turbulence data to show the augmentation levels due to turbulence. The augmentation levels at exit Ma 0.55 are shown in Figure 1.12. On the suction side before the transition, the turbulence augments the heat transfer on average by 27% and 22% for turbulence levels of 12% and 14%, respectively. The pressure side shows an average augmentation level of 11% and 8% for turbulence levels of 12% and 14%, respectively. A maximum augmentation level of 60% occurs just downstream of the leading edge and corresponds to the decelerating flow region. Similar levels and trends in augmentation occur for both turbulence levels.

Figures 1.13 and 1.14 show how the experimental data compares with the turbulent and laminar flat plate heat transfer correlations on the suction and pressure side of the blade, respectively. On the suction side (Fig. 1.13), boundary layer appears to be somewhere between fully laminar and fully turbulent before the flow transitions near the throat. The augmentation on the suction side can also be seen since the high turbulence levels fall closer to the turbulent correlation than the baseline, 2% turbulence case. On the pressure side (Fig. 1.14), the measured heat transfer is near the turbulent correlation, indicating that the pressure side boundary layer is fully turbulent.

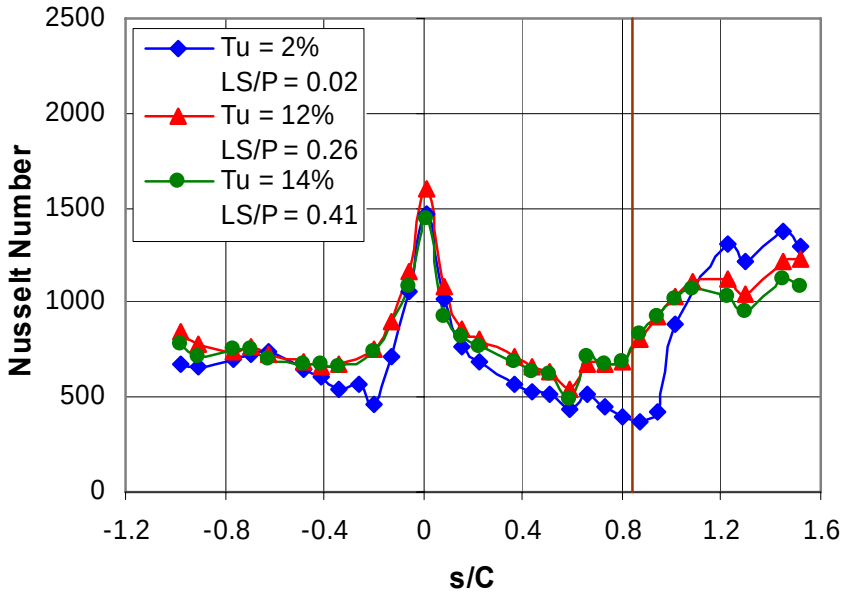

Figure 1.11. Heat transfer distribution at exit Ma 0.55

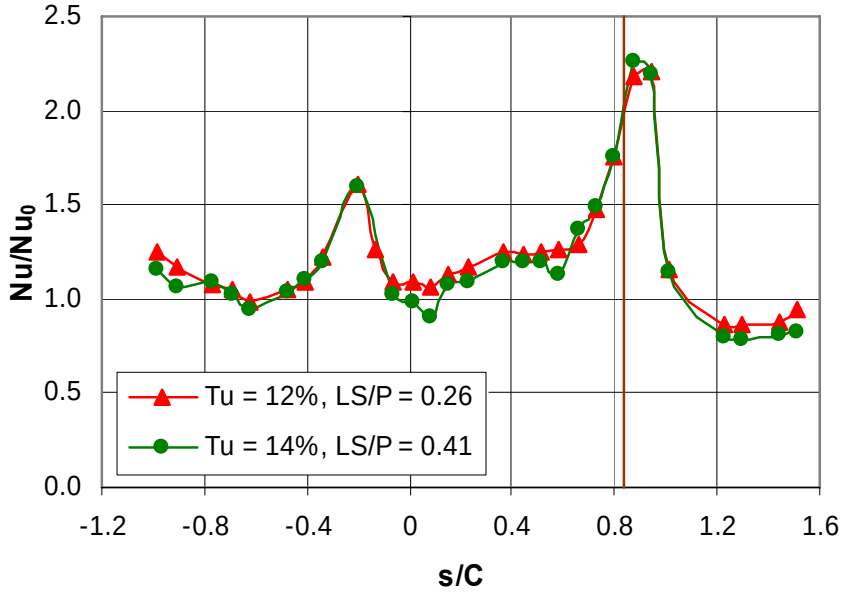

Figure 1.12. Heat transfer augmentation at exit Ma 0.55

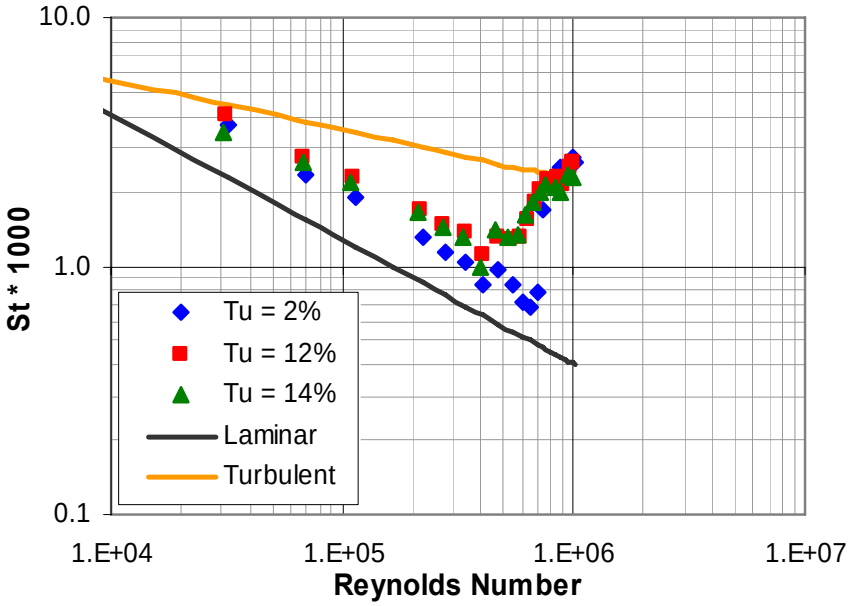

Figure 1.13. Suction side data compared to the flat plate correlation at exit Ma 0.55

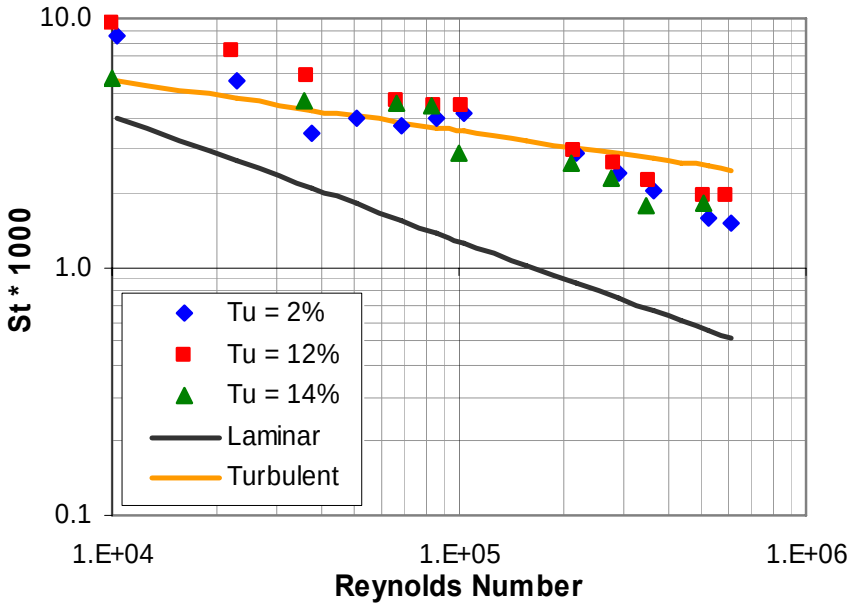

Figure 1.14. Pressure side data compared to the flat plate correlation at exit Ma 0.55

Figure 1.15 shows the heat transfer distribution plots for each turbulence level at exit Ma 0.78. Similar trends in augmentations are observed between the exit Ma 0.55 and 0.78 cases. Again, the boundary layer transition on the suction side occurs just upstream of the throat at s/C = 0.80 for each turbulence level. Since the transition locations for each turbulence level occur at the same point on the blade, the transition lengths for each turbulence level are roughly the same.

On the pressure side, higher augmentation levels can be seen. The low freestream turbulence data shows a local peak in the heat transfer data downstream of the leading edge on the pressure side at s/C = -0.26. Local peaks in heat transfer on the pressure side have been observed by Consigny and Richards [1.3], Arts et al. [1.4] and Giel et al. [1.5]. This location is corresponds to the location of the flow deceleration and has been hypothesized by Arts et al. [1.4] and Giel et al. [1.5] to be caused by local flow separation. At the higher turbulence levels, the local peak appears to be diminished. Unfortunately, the gauge located at the peak was damaged after completing the heat transfer measurements at low freestream turbulence. However, the gauges surrounding the damaged gauge do not appear to indicate that a peak is present when the turbulence levels are increased.

The heat transfer augmentation plots at exit Ma 0.78 are provided in Figure 1.16 and show the increase in heat transfer due to the turbulence. Again, similar trends between the exit Ma 0.55 and exit Ma 0.78 cases are observed. The average augmentation levels on the suction

side are 35% before transition occurs for both turbulence levels. On the pressure side, an average augmentation of 22% and 25% is observed for the 12% and 14% turbulence levels, respectively. The largest augmentation on the pressure side is 84% and occurs just downstream of the leading edge where the flow decelerates.

Figures 1.17 and 1.18 provide the comparisons with the flat plate correlations for the suction side and the pressure side, respectively. On the suction side (Fig. 1.17), the data lies between the laminar and turbulent correlations before the transition occurs. The data follows the trend of the laminar correlation before transitioning. The augmentation due to turbulence is also shown before transition and all three experiments go to similar Stanton numbers after the boundary layer transition. On the pressure side (Fig. 1.18), the data starts above the turbulent correlation and then decays below the turbulent correlation. The data having a steeper slope than the turbulent correlation might suggest that the boundary layer is attempting to relaminarize. From the acceleration parameter in Figure 1.10, the acceleration parameter is above the critical value on the majority of the pressure side, which supports the possibility of relaminarization occurring.

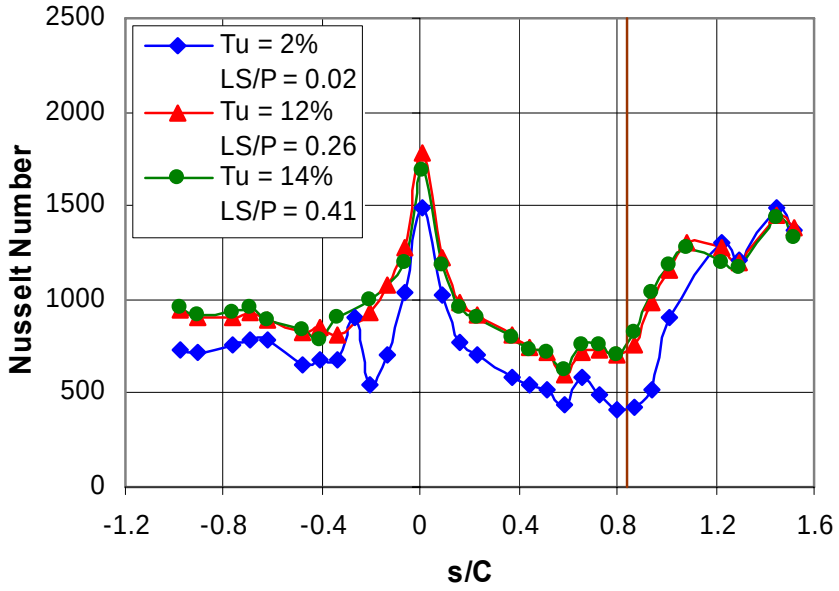

Figure 1.15. Heat transfer distribution at exit Ma 0.78

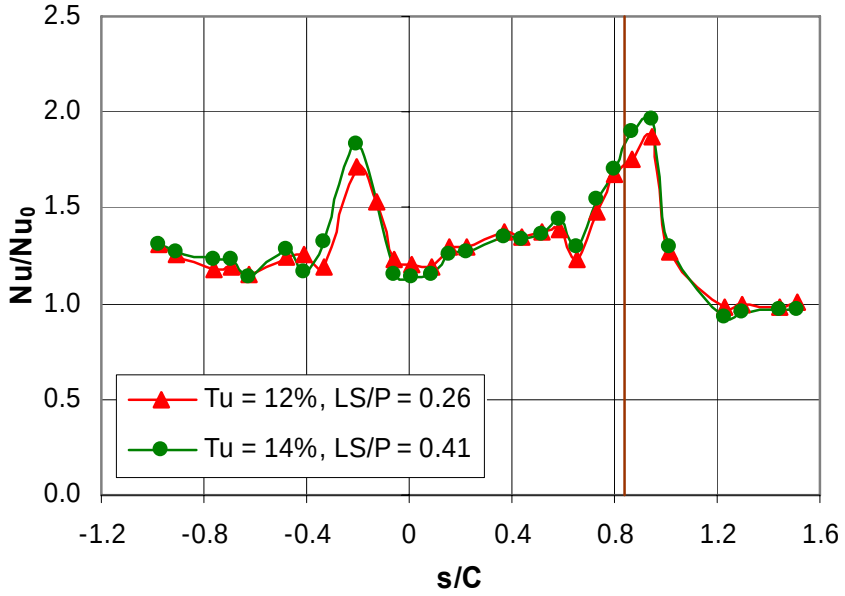

Figure 1.16. Heat transfer augmentation at exit Ma 0.78

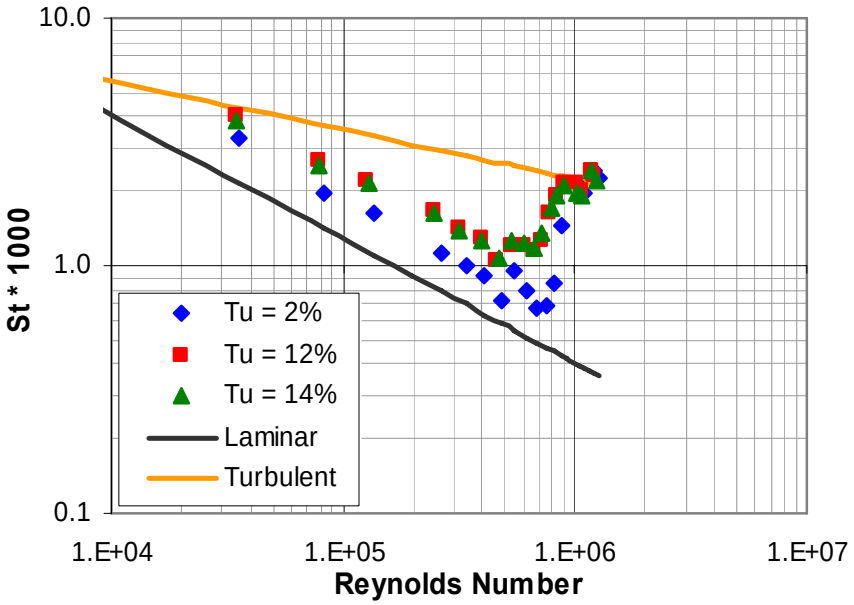

Figure 1.17. Suction side data compared to the flat plate correlation at exit Ma 0.78

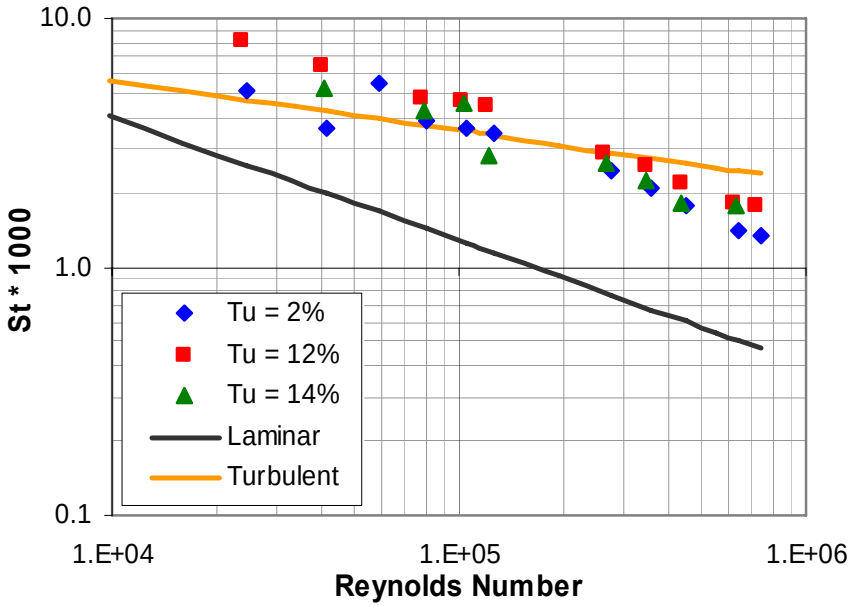

Figure 1.18. Pressure side data compared to the flat plate correlation at exit Ma 0.78

The exit Ma 1.03 case provides the most interesting data of the conditions tested. Up to this point the data presented for the exit Mach 0.55 and 0.78 conditions has behaved as expected and shows trend similar to what other researchers have observed.

The heat transfer distribution along the blade surface for exit Ma 1.03 is provided in Figure 1.19. On the suction side of the blade, the turbulence augments the heat transfer up to the transition location at s/C = 0.58. For the 2% turbulence case, the boundary layer transition is sustained for a significant distance over the blade. The length of this transition is significantly longer that the transition lengths observed at exit Mach 0.55 and 0.78 since the flow is accelerating. The 12% and 14% turbulence cases show what appears to be the start of transition at s/C = 0.58. However, the increase in heat transfer is very gradual for both the 12% and 14% turbulence cases. A sharp rise in heat transfer occurs at s/C = 1.01 which corresponds to where the flow for the Mach 1.03 tests begins to decelerate. On the pressure side, the local peak cause by the possible flow separation has increased in amplitude, as compared to the 0.55 and 0.78 Mach number cases.

A difference in the augmentation levels for the mesh grid and the bar gird occurs at the high exit Mach number case. The 12% turbulence data shows a higher augmentation levels on both the pressure and suction sides of the blade than the 14% turbulence data. Since the turbulence levels for each high freestream turbulence test are approximately the same, the length

scales are the only difference between the tests. It appears that for the exit Mach 1.03 tests, the smaller length scale augments the heat transfer more than larger length scale.

Figure 1.20 shows the augmentation plots for exit Mach 1.03. Augmentation on the suction side is shown before the flow transitions. As previously mentioned, the augmentation levels between the 12% and 14% turbulence tests differ significantly. The average augmentation on the suction side before transition is 27% for the 12% turbulence test and 12% augmentation for the 14% turbulence test. Once the flow transitions, the augmentation goes negative because the gradual transition at the high turbulence levels. On the pressure side, the average augmentation for 12% turbulence is 6% and -4% augmentation for the 14% turbulence. Maximum augmentation on the pressure side of 120% was measured for 12% turbulence and 110% for the 14% turbulence tests. Again, the maximum augmentation occurs at the location where the flow is decelerating.

Figures 1.21 and 1.22 provide the suction and pressure side comparisons with the flat plate correlations at exit Mach 1.03, respectively. Again, the data on the suction side (Fig. 1.21) lies between the laminar and turbulent correlations. The augmentation caused by increasing the turbulence level can also be seen along with the transition locations. On the pressure side (Fig. 1.22), the exit Mach 1.03 data falls along the turbulent correlation as did the exit Mach 0.55 and 0.78 data. The one exception is the valley in the heat transfer data at $s/C = -0.13$ that lies close to the laminar correlation. This valley is just upstream of the deceleration region. The heat transfer being close to the laminar correlation suggests that the flow is laminar at this location.

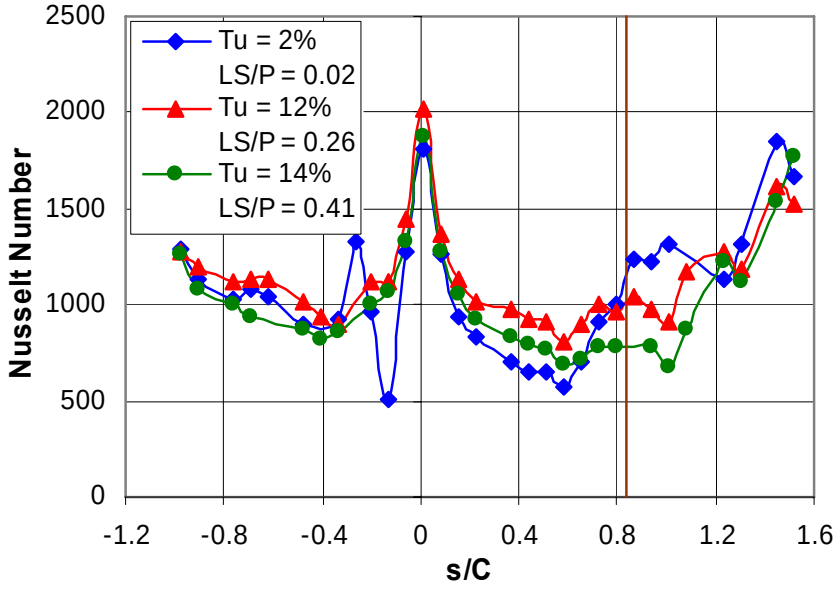

Figure 1.19. Heat transfer distribution at exit Ma 1.03

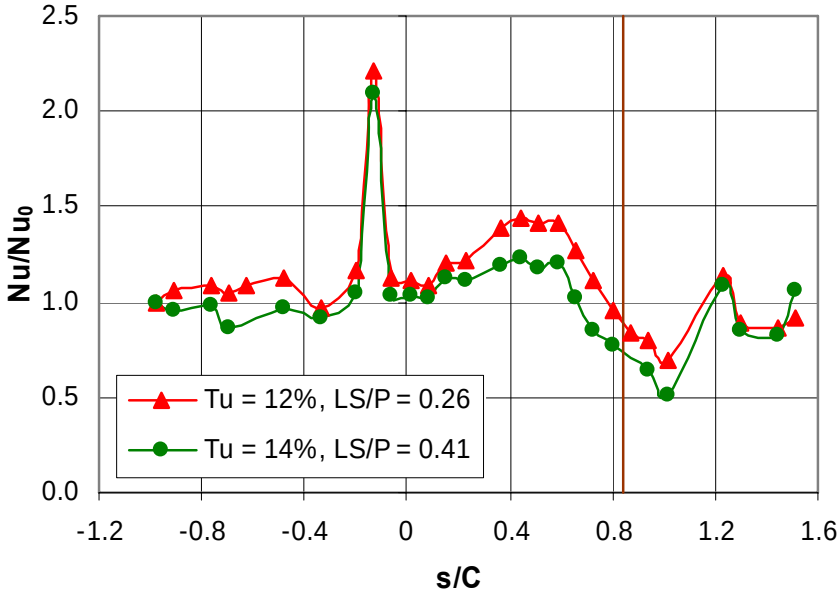

Figure 1.20. Heat transfer augmentation at exit Ma 1.03

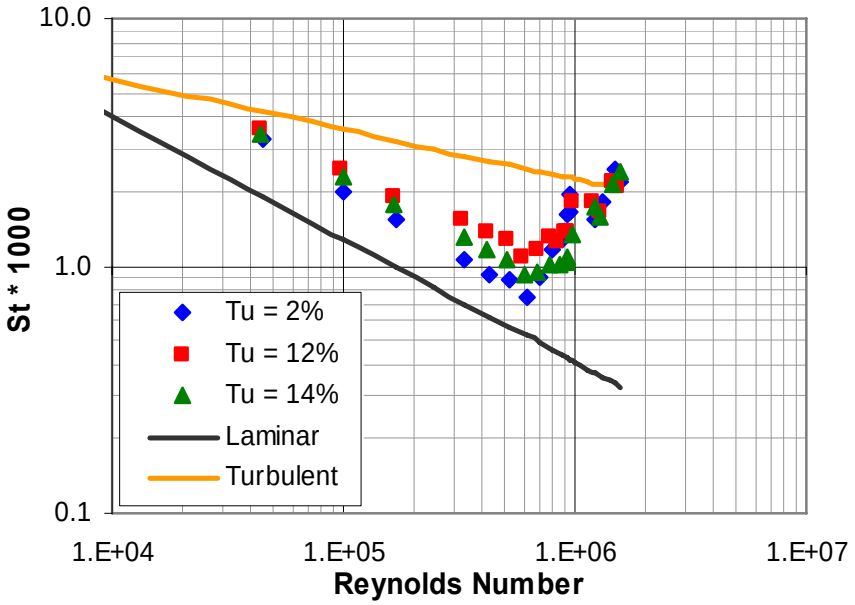

Figure 1.21. Suction side data compared to the flat plate correlation at exit Ma 1.03

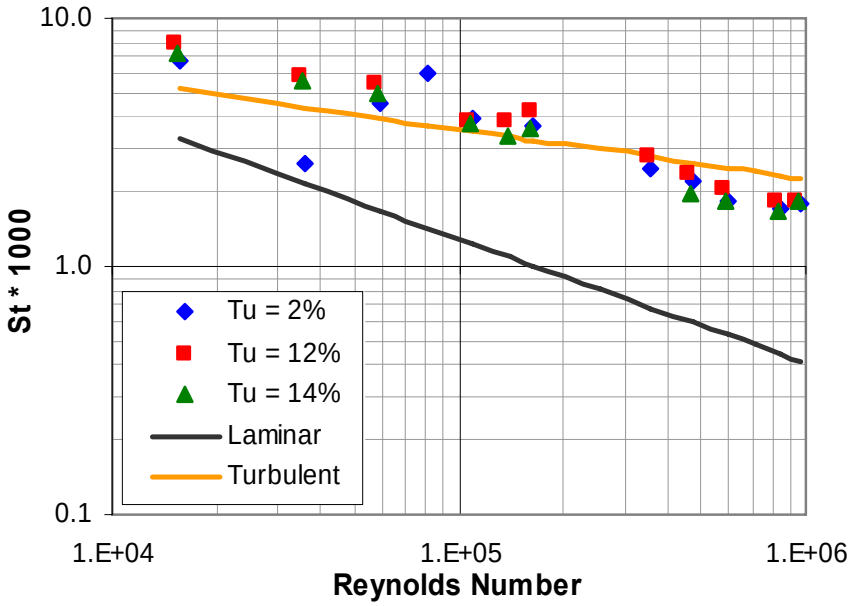

Figure 1.22. Pressure side data compared to the flat plate correlation at exit Ma 1.03

Effect of Reynolds Number

Because of facility constraints, an increase in the exit Mach number was coupled to an increase in the exit Reynolds number. To remain consistent with the previous sections, the data will be compared by stating the Mach number. The actual Reynolds numbers measured for each test is provided in Table 3. The Nusselt number distributions showing the effect of increasing the Reynolds number at turbulence levels of 2%, 12%, and 14% are shown in Figures 1.23, 1.24, and 1.25.

The 2% turbulence data plotted in Figure 1.23 shows several different trends. As expected, there is an overall increase in heat transfer due to the increase in Reynolds number. The increase in heat transfer is not significant between the exit Mach 0.57 and 0.76 cases. A larger increase in heat transfer occurs between the exit Mach 0.76 and 1.03. The increase in exit Reynolds number also causes an earlier boundary layer transition. Again, there is a large shift in the transition location between the exit Mach 0.76 and 1.03 tests and a negligible shift between the exit Mach 0.57 and 0.76 tests. On the pressure side, the local peak caused by separation increases in amplitude as the Reynolds number increases and was also observed by Consigny and Richards [1.3].

The 12% turbulence cases shown in Figure 1.24 also indicates an increase in heat transfer with increasing the Reynolds number all over the blade surface, except after the throat for the exit Mach 1.03 case. An increase in the heat transfer with Reynolds number is not seen near the throat since the boundary layer transition is gradual at exit Mach 1.03.

Figure 1.25 provides the 14% turbulence cases and also shows the increase in heat transfer with increasing the Reynolds number. A large increase in heat transfer is observed between the exit Mach 0.55 and 0.78 cases. Between the exit Mach 0.78 and 1.01 cases there is only a slight increase in heat transfer with Reynolds number except at the leading edge. Near the throat, there is no increase in heat transfer with Reynolds number due to the slow transition.

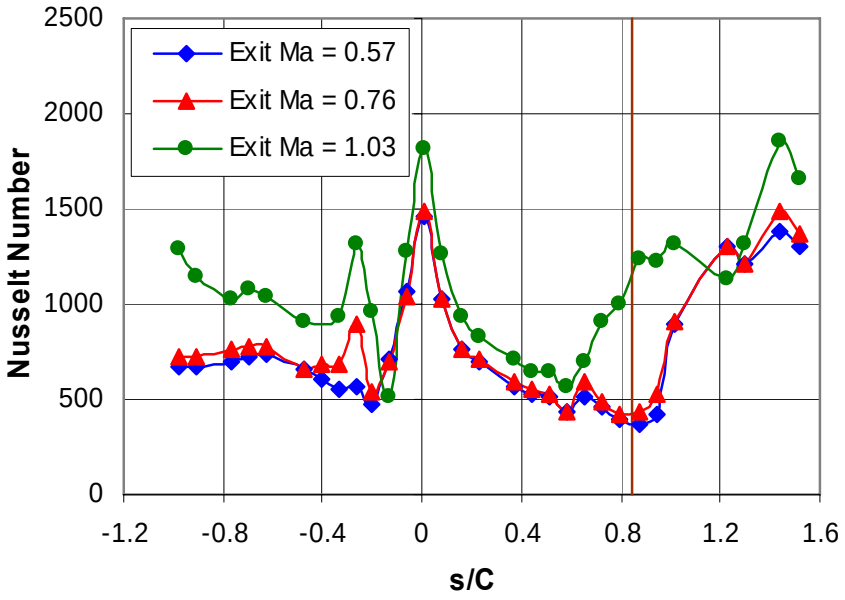

Figure 1.23. Heat transfer distribution at Tu = 2%

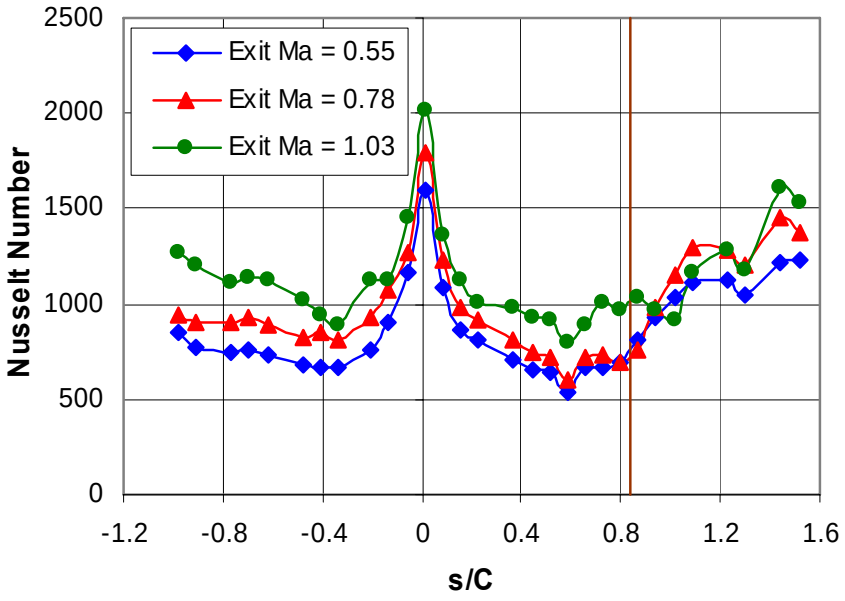

Figure 1.24. Heat transfer distribution at Tu = 12%

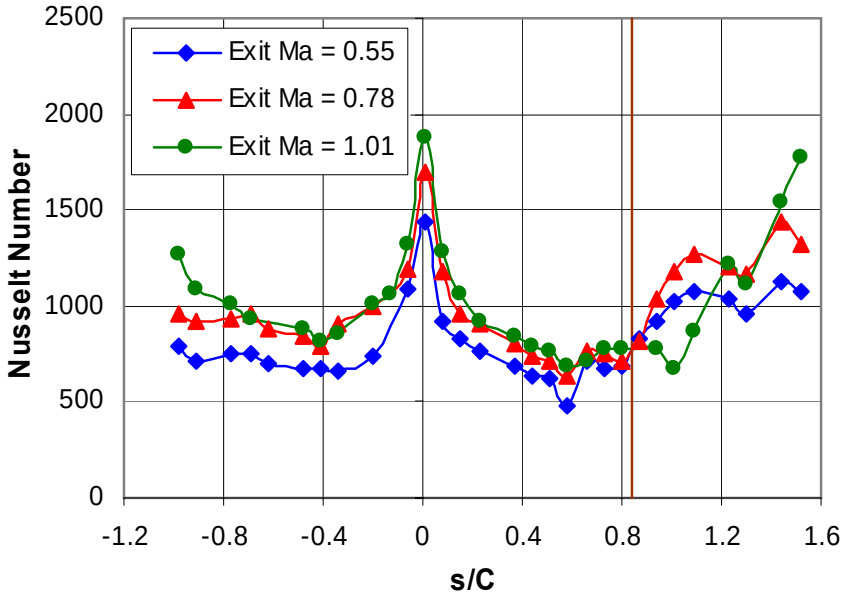

Figure 1.25. Heat transfer distribution at Tu = 14%

Effect of Length Scale

As shown in Figures 1.11, 1.15, and 1.19, the heat transfer is augmented more at the leading edge with the 12% turbulence than the 14% turbulence. Since the turbulence levels are similar, the difference in heat transfer is caused by the size of the turbulence length scale. At similar turbulence levels, the heat transfer is augmented more at the leading edge if the size of the length scale is smaller. Van Fossen et al. [1.17] also observed that decreasing the length scale will increase the heat transfer augmentation at the leading edge. Both the turbulence intensity and the length scale size have an effect on the heat transfer in the stagnation region.

The effect of the length scale also appears at the exit Mach 1.03 conditions as shown in Figures 1.19 and 1.20. On both the pressure side and suction side of the blade, the 12% turbulence shows higher augmentation levels than the 14% turbulence. The only difference between the two tests is the size of the turbulent eddy.

Leading Edge Correlation

The experimental data at the leading edge was compared to the stagnation region heat transfer correlation for elliptical leading edges developed by Van Fossen et al. [1.17]. The stagnation region heat transfer correlation takes into account the turbulence intensity, length scale, leading edge diameter and Reynolds number and is provided by,

$$\frac{Fr_{Tu}}{Fr_{lam}} = 0.00851\sqrt{Tu\,\mathrm{Re}_{d,in}^{0.8}\left(\frac{\Lambda_x}{d}\right)^{-0.574}} + 1.0 \qquad (5)$$

The plot of the correlation and the data are provided in Figure 1.26. The experimental leading edge heat transfer data was converted into a Frossling number given by,

$$Fr_{Tu} = Nu \cdot \frac{(d/C)}{\sqrt{\mathrm{Re}_{d,in}}} \qquad (6)$$

From the blade geometry, the leading edge approximated to a ellipse with an aspect ratio of 2.25:1 where $Fr_{lam} = 0.811$. The experimental data at the leading edge compares rather well with the Van Fossen correlation. All of the data follows the same trend as the correlation and lies within ±10% of the Van Fossen correlation. The experimental data also shows good agreement with the results reported by Giel et al. [1.5].

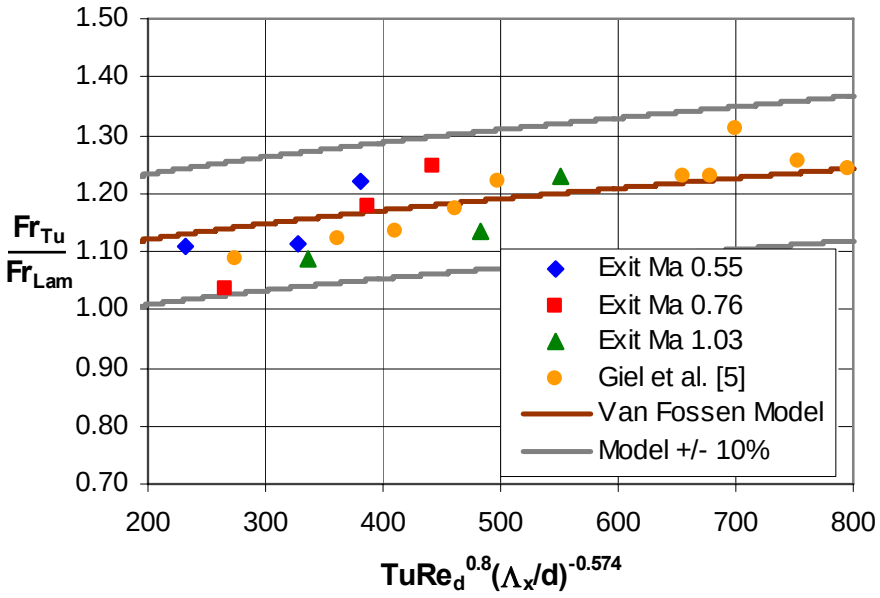

Figure 1.26. Van Fossen correlation comparison

TEXSTAN Comparison

The experimental data was compared with surface heat transfer predictions made using academic version of TEXSTAN developed by Crawford [1.18]. To model the flow through the blade passages, the two-equation Lam-Bremhorst turbulence model was used with the Schmidt-Patankar transition model. A constant surface temperature boundary condition was applied to the blade and the constant turbulence kinetic energy was set throughout the computational domain by freezing the turbulence dissipation rate.

At low freestream turbulence, the TEXSTAN prediction matches the experimental data well as shown in Figure 1.27. The suction side heat transfer prediction matches levels and transition location of the data very well. On the pressure side, TEXSTAN slightly underpredicts the heat transfer and does not predict the local peak near the leading edge.

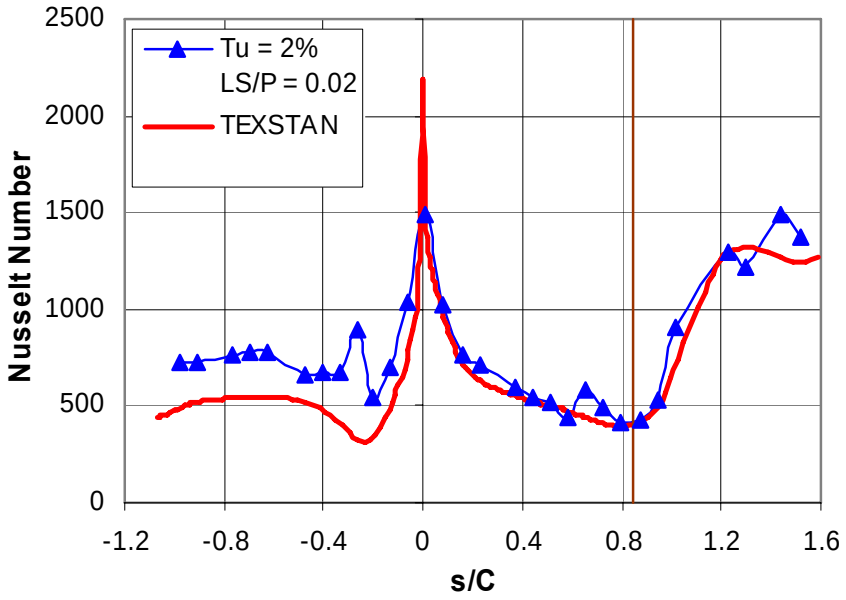

Figure 1.27. Texstan prediction at exit Ma 0.78, 2% Tu

At higher turbulence levels, TEXSTAN overpredicted the heat transfer on both the pressure and suction sides as shown in Figure 1.28. The suction side prediction appears to be fully turbulent with the data only coming close to the prediction after the transition. The pressure side is also well overpredicted. As shown in Figure 1.18, the experimental data falls close to the turbulent flat plate correlation and the TEXSTAN prediction is well above the correlation. The leading edge heat transfer is also overpredicted. Similar trends were observed with the predictions at exit Ma 0.55 and 1.03.

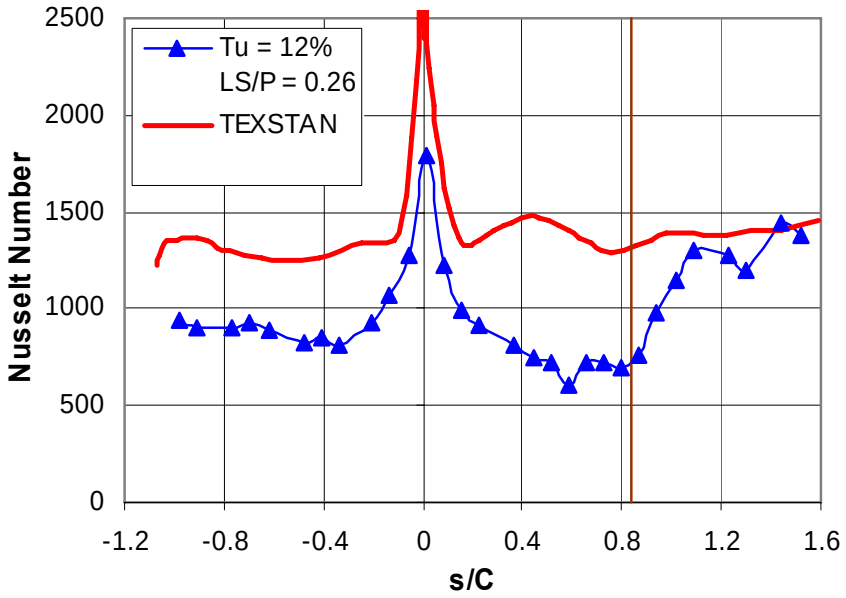

Figure 1.28. Texstan prediction at exit Ma 0.78, 12% Tu

Conclusions

Aerodynamic and heat transfer measurements were made on a turbine blade at flow conditions representative of engine operating conditions. High levels of freestream turbulence were generated by using passive turbulence grids that produced similar turbulence levels, but different length scales. Increasing the turbulence level was observed to augment the heat transfer over the blade surface.

The turbulence augmentations for the two high freestream turbulence levels with different length scales were almost identical except at the leading edge for the exit Mach 0.55 and 0.78 cases. For the exit Mach 1.03 cases, the turbulence was augmented more for the smaller turbulence length scale. The boundary layer transition was somehow delayed on the suction side at the higher turbulence levels. Increasing the freestream turbulence was observed to not significantly influence the location of boundary layer transition.

As expected, increasing the exit Reynolds number was shown to increase the heat transfer levels and cause earlier boundary layer transition. The boundary layer transition was observed to be influenced primarily by the Reynolds number of the flow. An increase in the exit Reynolds

(Mach) number caused the boundary layer to transition closer to the leading edge. The local peak on the pressure side increased with increasing the Reynolds number for the baseline case.

Several comparisons were made between the data using the analytical flat plate correlations, leading edge correlations developed by Van Fossen and the TEXSTAN predictions. The heat transfer data generally lied between the flat plate correlations for laminar and turbulent flows and showed good agreement with Van Fossen's leading edge correlation. The TEXSTAN prediction accurately modeled the heat transfer at low freestream turbulence levels, but was found to significantly overpredict the heat transfer levels at high turbulence levels.

Acknowledgements

This work was sponsored by Solar Turbines Inc. We would also like to express our gratitude to Dr. Richard Anthony and Dr. Marcus Polanka of the Air Force Research Laboratory, Wright-Patterson AFB for their help with manufacturing and implementation of the thin film gauges.

References

[1.1] Zimmermann, D. R., 1979, "Laser anemometer measurements at the exit of a T63-C20 combustor," NASA CR-159623.

[1.2] Van Fossen, G. J. and Bunker, R. S., 2000 "Augmentation of stagnation heat transfer due to turbulence from a DLN can combustor," ASME Paper No. 2000-GT-215.

[1.3] Consigny, H. and Richards, B.E., 1982, "Short Duration Measurements of Heat-Transfer Rate to a Gas Turbine Rotor Blade," *ASME J. Eng. Power*, **104**, pp. 542–551.

[1.4] Arts, T., Duboue, J.-M. and Rollin, G., 1998, "Aerothermal Performance Measurements and Analysis of a Two-Dimensional High Turning Rotor Blade," *ASME J. Turbomach.*, **120**, pp. 494-499.

[1.5] Giel, P. W., Boyle, R. J., and Bunker, R. S., 2004, "Measurements and Predictions of Heat Transfer on Rotor Blades in a Transonic Turbine Cascade," *ASME J. Turbomach.*, **126**, pp. 110-121.

[1.6] Schultz, D.L., and Jones, T.V., 1973, "Heat Transfer Measurements in Short Duration Hypersonic Facilities," AGARD AG-165.

[1.7] Doorly, J.E., and Oldfield, M.L.G., 1987, "The Theory of Advanced Multi-Layer Thin Film Heat Transfer Gages," *Intl. J. Heat and Mass Transfer*, **30**, No. 6, pp. 1159–1168.

[1.8] Dunn., M.G., 1995, "The Thin-Film Gage," von Karman Institute for Fluid Dynamics, Lecture Series 1995-01.

[1.9] Joe, C.R., 1997, "Unsteady Heat Transfer on the Turbine Research Facility at Wright Laboratory," PhD Dissertation, Syracuse University.

[1.10] Cress, R.D., 2006, "Turbine Blade Heat Transfer Measurements in a Transonic Flow Using Thin Film Gages," Master's Thesis, Virginia Polytechnic Institute and State University.

[1.11] Moffat, R. J., 1988, "Describing Uncertainties in Experimental Results," *Exp. Thermal and Fluid Science*, 1988, pp. 3-17.

[1.12] Baines, W.D. and Peterson, E.G., 1951, "An Investigation of Flow Through Screens," *Trans. of the ASME*, July 1951, pp. 467-480.

[1.13] Nix, A.C., Smith, A.C., Diller, T.E., Ng, W.F. and Thole, K.A., 2002, "High Intensity, Large Length-Scale Freestream Turbulence Generation in a Transonic Turbine Cascade," ASME GT-2002-30523.

[1.14] Jones and Launder, B. E., "The Prediction of Laminarization with a Two-Equation Model of Turbulence," *Intl. J. Heat and Mass Transfer*, **15**, 1972, pp. 301-314.

[1.15] Mayle, R.E., 1991, "The Role of Laminar-Turbulent Transition in Gas Turbine Engines," *ASME J. Turbomach.*, **113**, pp. 509-537.

[1.16] Zhang, J., and Han, J.-C., 1994, "Influence of Mainstream Turbulence on Heat Transfer Coefficient From a Gas Turbine Blade," *ASME J. Heat Transfer*, **116**, pp. 896 - 903

[1.17] Van Fossen, G. J., Simoneau, R. J., and Ching, C. Y., 1995, "Influence of Turbulence Parameters, Reynolds Number, and Body Shape on Stagnation-Region Heat Transfer," *ASME J. Heat Transfer*, **117**, pp. 597-603.

[1.18] Crawford, M.E., 1986, "Simulation Codes for Calculation of Heat Transfer to Convectively-Cooled Turbine Blades," *Convective Heat Transfer and Film Cooling in Turbomachinery*, VKI Lecture Series 1986-06.

Appendix A

Turbine Blade Geometry

The turbine blade geometry used in these experiments is representative of a first stage turbine blade. This blade has a high turning angle of 107.5° to extract a large amount of work from the stage. To match the desired exit Reynolds numbers, the blade has been scaled two times its original size. The scaling resulted in a blade with a true chord of 2.75 in. and a blade pitch of 2.29 in. The blade has been angled at 40° relative to the flow of in the cascade so that the inlet velocity vectors would match the orientation in the engine. The span of the blade is 6". A profile view of the turbine blade is shown in Figure A-1. Table A-1 provides a summary of the blade geometry.

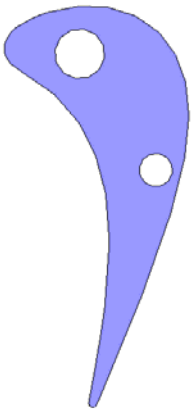

Figure A-1. Profile view of turbine blade

Table A-1. Turbine blade geometry

True Chord	2.75 in.
Axial Chord	1.39 in.
Pitch	2.29 in.
Span	6.00 in.
Turning Angle	107.5°

From the blade geometry and the test section dimensions, the number of blades that could be used in the cascade was set. A total of 7 full blades and two partial blades were used to create

the blade cascade. The blades were numbered starting with the lower left blade of the cascade. Blade 4 would be the blade instrumented with pressure taps for the local Mach number distributions and with thin film gauges to make the heat transfer measurements. The suction side of blade 3 and the pressure side of blade 5 are instrumented with pressure taps.

On the end wall of the test section two slots were machined so that the flow fields entering the blade passages could be measured. One slot is angled parallel to the inlet of the cascade. The other slot is perpendicular to the flow and is located 5 in. upstream of the leading edge of blade 4. Both slots are 4.25 in. long and centered about the leading edge of blade 4. A schematic of the blade test section showing the blades and the measurement slots are shown in Figure A-2.

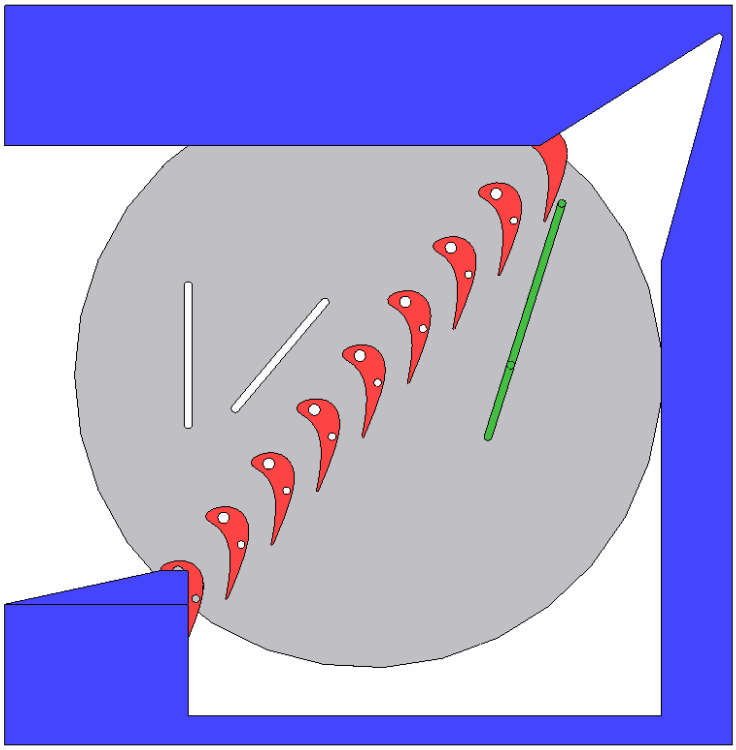

Figure A-2. Schematic of test section showing the blade orientation

Wind Tunnel

The test section with the blade cascade was installed into the Virginia Tech transonic cascade wind tunnel. The wind tunnel is a blow-down facility that is capable of supplying

heated air to the test section. A compressor is used to pressurize air in two large air tanks up to 200 psi prior to starting a run. An open-close valve and a proportional control valve are used to regulate the flow of air into the test section. Once the air passes through the valves, the air goes through a passive heat exchanger that consists of two bundles of copper tubes. The air exiting the heat exchanger can be up to 120°C. Before beginning the test the copper tubes are heated by cycling hot air through the heater loop. The air is heated with electric heaters. After the air passes through the heat exchanger, the air goes through several fitting and a contraction before entering the test section. The air then is exhausted to the atmosphere. A schematic of the wind tunnel is shown in Figure A-3.

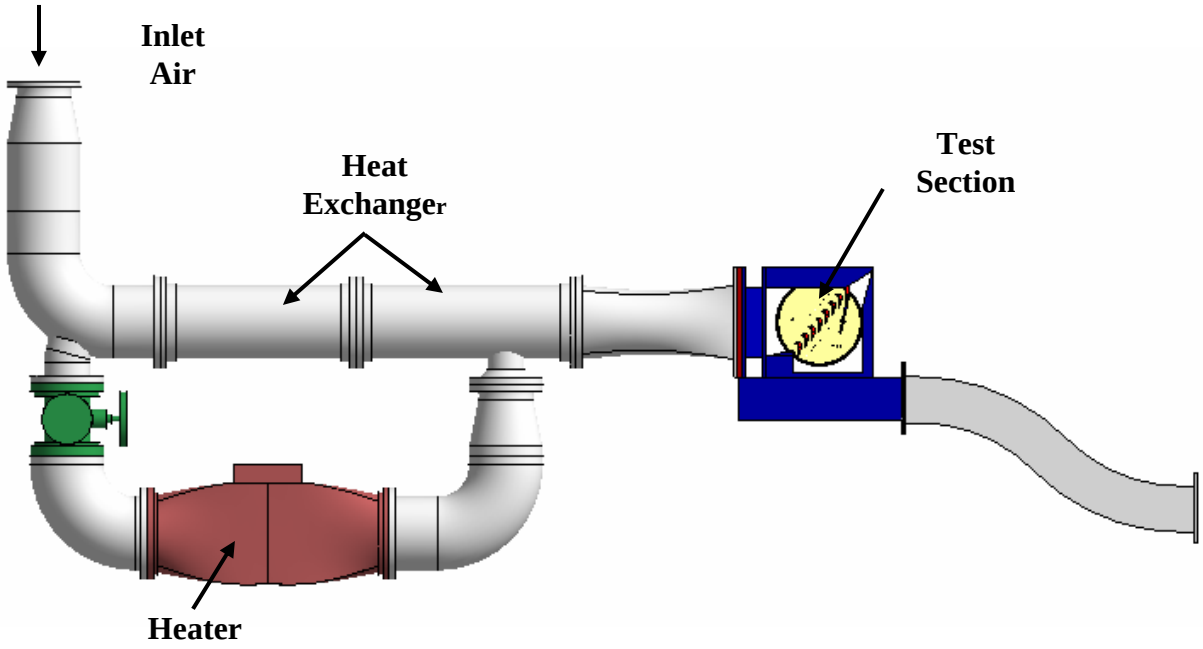

Figure A-3. Schematic of Virginia Tech transonic wind tunnel

A steady inlet and exit Mach number can be maintained for up to 20 seconds in the test section after an initial transient period. This allowed for pressure measurements to be made for that period of time. A shorter period of time was available to make heat flux measurements since the air temperature constantly decreasing. Heat transfer measurements are typically made in the first 5 to 10 seconds after the run begins. A graph of the time history of the test section pressure and air temperature is shown in Figure A-4.

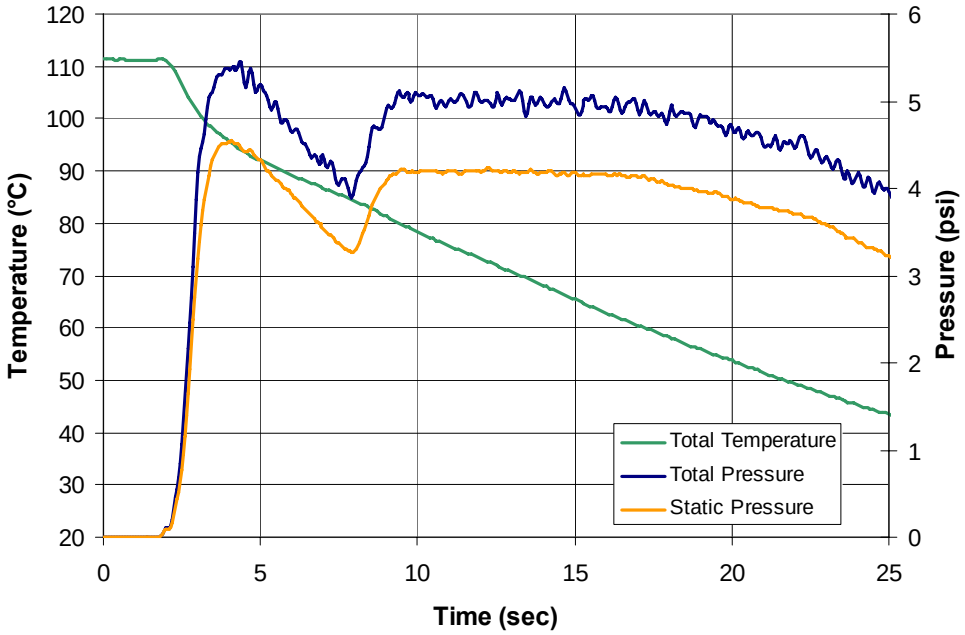

Figure A-4. Plot of the typical pressure and temperature time history during an experiment

Appendix B Local Mach Number Distribution

Pressure Tap Layout

Pressure taps were installed on the turbine blades by cutting a slot in the blade. Small tubes were installed into the slots and an adhesive was used to hold the tube in place. The adhesive was sanded off to make a smooth blade surface. A hole was drilled into the tube that was normal to the blade surface at the midspan of the blade. This hole allowed the static pressure at the surface of the blade to be measured. The blade 4 was instrumented with a total of twenty-seven pressure taps with nine taps on the pressure side of the blade, seventeen taps on the suction side and one tap near the leading edge. Blade 3 was instrumented with seventeen taps on the suction side and one tap at the leading edge. Blade 5 was instrumented with nine taps on the pressure side and one tap at the leading edge. Blade 4 was measure the static pressure distribution. Blades 3, 4 and 5 were used to check the periodicity of the flow through the blade passages.

Static pressure taps were also installed on the end wall of the cascade at the inlet of the passages and at the exit of the passages. At the inlet, 12 end wall taps were placed 0.5C upstream of the cascade inlet and spaced 0.75 in. apart. There were also 12 wall taps installed downstream of the cascade exit at the same spacing as the inlet taps. The end wall taps were used to measure the uniformity of the inlet and exit flows. Figure B-1 shows the layout of the blade pressure taps, and the inlet and exit static taps in the cascade. A picture of the pressure taps instrumented on the blade are provided in Figure B-2.

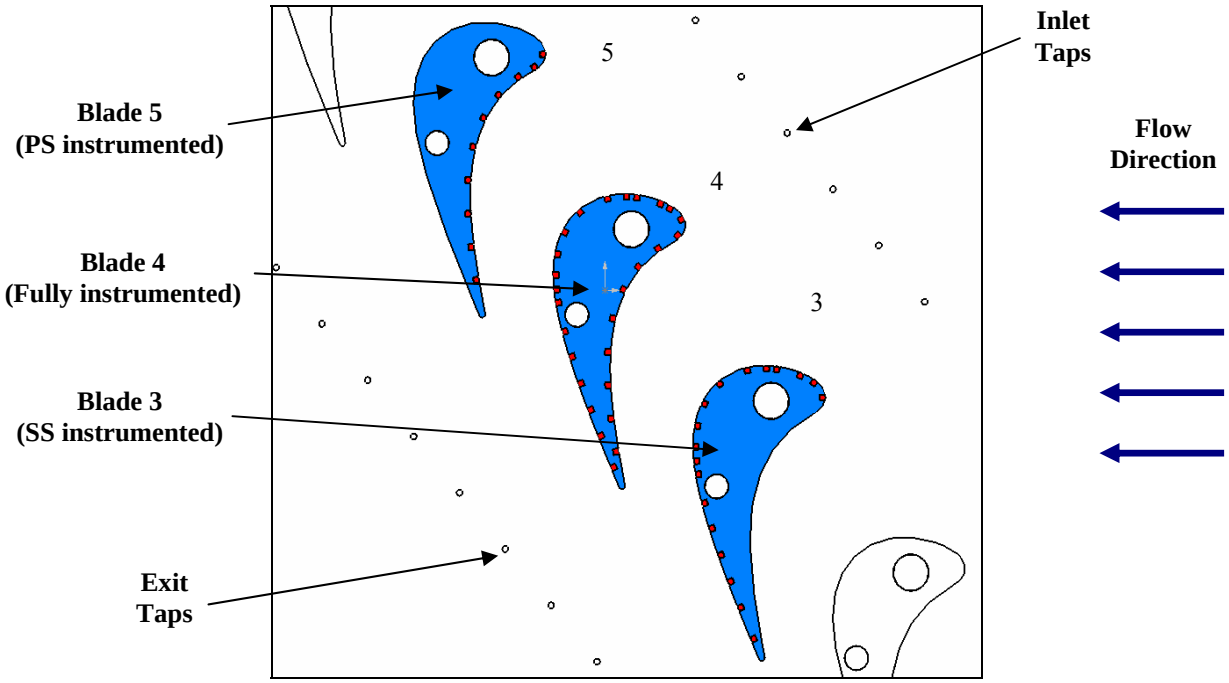

Figure B-1. Schematic showing the pressure tap locations on the blade

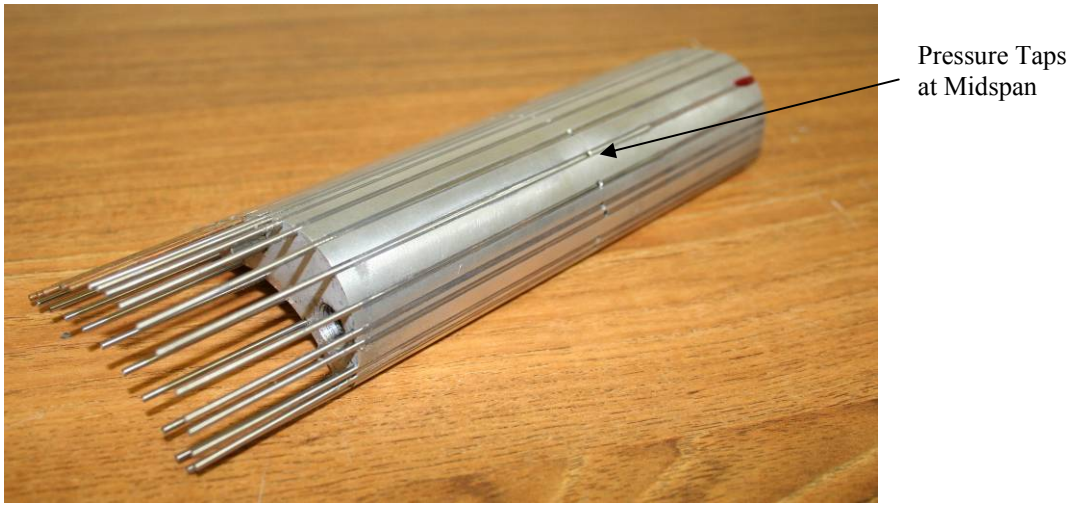

Figure B-2. Picture of the pressure taps instrumented on blade 4

Static Pressure Measurement Technique

A PSI 8400 System was used to collect the static pressure distribution on the blade during the run. A total of thirty-two pressure measurements could be made simultaneously and the pressure data was typically collected at 20 Hz. The static pressure data from each pressure tap was converted into a pressure ratio using the total pressure of the flow measured with a Pitot-

static probe located upstream of the cascade inlet. With the pressure ratio, the local Mach number could then be calculated by using equation B-1,

$$Ma = \sqrt{\frac{2}{\gamma - 1} \cdot \left(PR^{\frac{\gamma - 1}{\gamma}} - 1 \right)} \qquad \text{(B-1)}$$

where PR is the pressure ratio and γ is the specific heat ratio of air. It was assumed that there were no losses through the blade passages, so the total pressure remained constant. Once the Mach numbers were calculated, the data was typically averaged over 10 seconds of the run when the exit Mach number was steady.

The local Mach number distribution on the blade was also examined by calculating the acceleration parameter. From the local Mach number distribution, the local velocities and densities were calculated at each point on the blade. The acceleration parameter is a nondimensional way of indicating how the flow is accelerating over the blade and is provided in equation B-2,

$$k = \frac{\nu}{U^2} \cdot \frac{dU}{ds} \qquad \text{(B-2)}$$

where ν is the kinematic viscosity, U is the local velocity and s is the surface distance from the leading edge. The acceleration parameter is useful in predicting boundary layer events such as relaminarization and separation.

Run Repeatability

Experiments to establish run to run repeatability were performed by making measurements multiple times at the same conditions. The run repeatability was check at each exit Mach number condition. From the experiments, it was observed that the each test had similar results. The only noticeable variation between tests occurs downstream of the blade passage throat (x/C = 0.84). After the throat, the flow is no longer bound by the blades and free expansion of the flow occurs. Any slight variation in the back pressure will cause a change in the local Mach number distribution downstream of the throat. Figure B-3 provides a plot showing the run to run repeatability of the experiments.

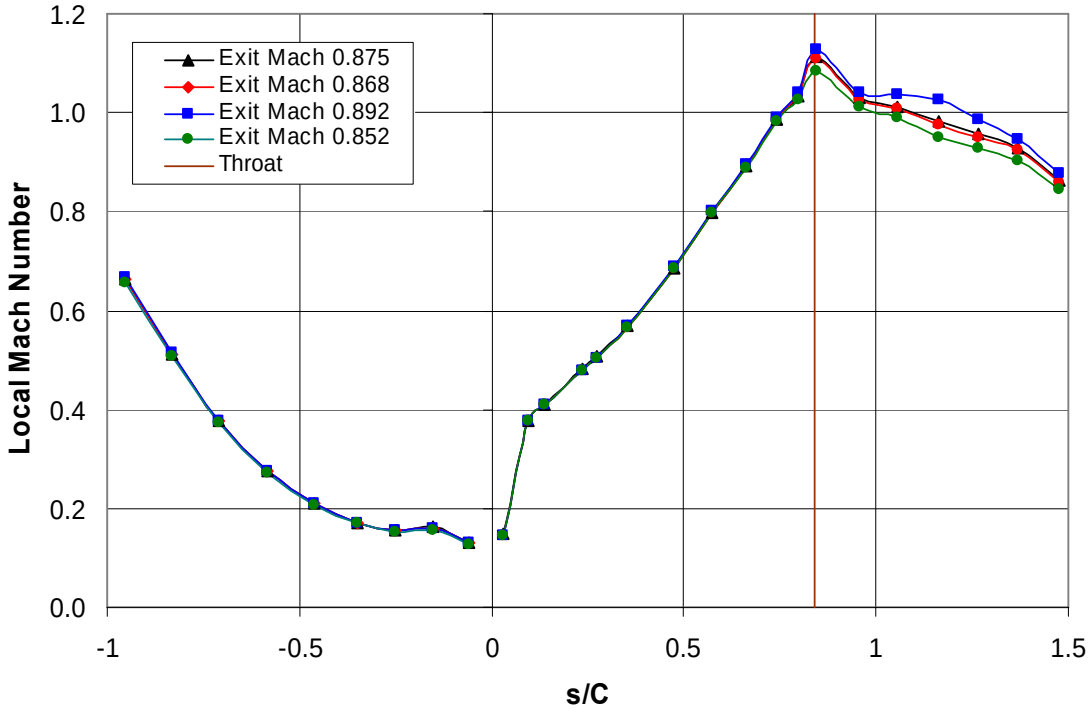

Figure B-3. Plot of the local Mach number over the blade surface for several runs at exit Ma 0.85

Local Mach Number Distribution

To measure the Mach number distribution, blade 4 was completely instrumented and experiments were performed at exit Mach numbers of 0.6, 0.85 and 1.1. Test runs were repeated several times for each case. The data shows similar local Mach number trends for each exit Mach number condition. On the pressure side, the flow accelerates initially before undergoing a slight deceleration period at x/C = -0.24. This deceleration occurs for each exit Mach number case. After the deceleration region, the flow accelerates over the remainder of the pressure surface. On the suction surface, the flow accelerates away from the leading edge up until the geometric throat at x/C = 0.84 for each exit Mach number. Exit Mach numbers of 0.85 and 1.1 exhibit the same exact acceleration on the pressure side and the suction side up to the throat. This occurs because the flow through the blade passages is choked. After the throat there is a difference in the two local Mach number distributions. A plot comparing the local Mach number distributions at the exit Mach numbers is provided in Figure B-4

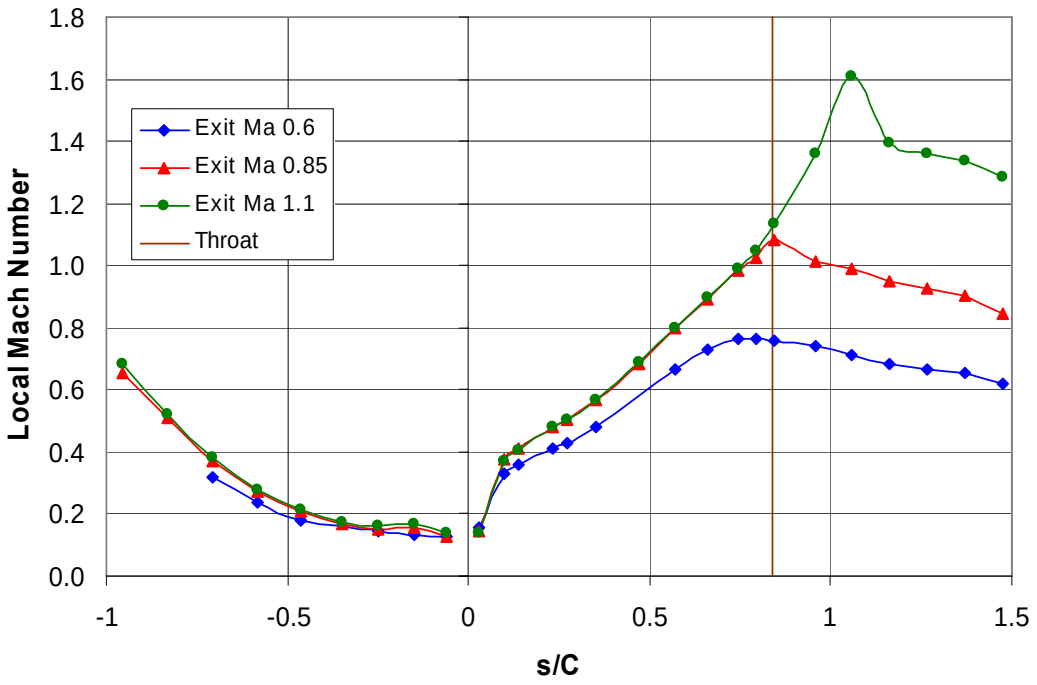

Figure B-4. Plot of the local Mach number distributions at the different exit Mach numbers

The flow was also analyzed by looking at the acceleration parameter plot. On the pressure side, the flow decelerates before undergoing a strong acceleration. According to Jones and Launder [F.1], Mayle [F.2], and Giel et al. [F.3], the boundary layer will relaminarize if the acceleration parameter exceeds 3×10^{-6}. There is a possibility of relaminarization on the pressure side since the acceleration parameter is above 3×10^{-6} for a large portion of the pressure surface. On the suction side, the flow accelerates up to the throat area. For the exit Mach 1.1 case, the flow continues to accelerate after the throat before beginning to decelerate. The 0.6 and 0.85 exit Mach cases show deceleration immediately after the throat. The acceleration levels on the suction side are much lower than the pressure side. The flow acceleration and deceleration can also be seen in local Mach number distribution plot of Figure B-4. Figure B-5 provides a plot of the acceleration parameter at each exit Mach number.

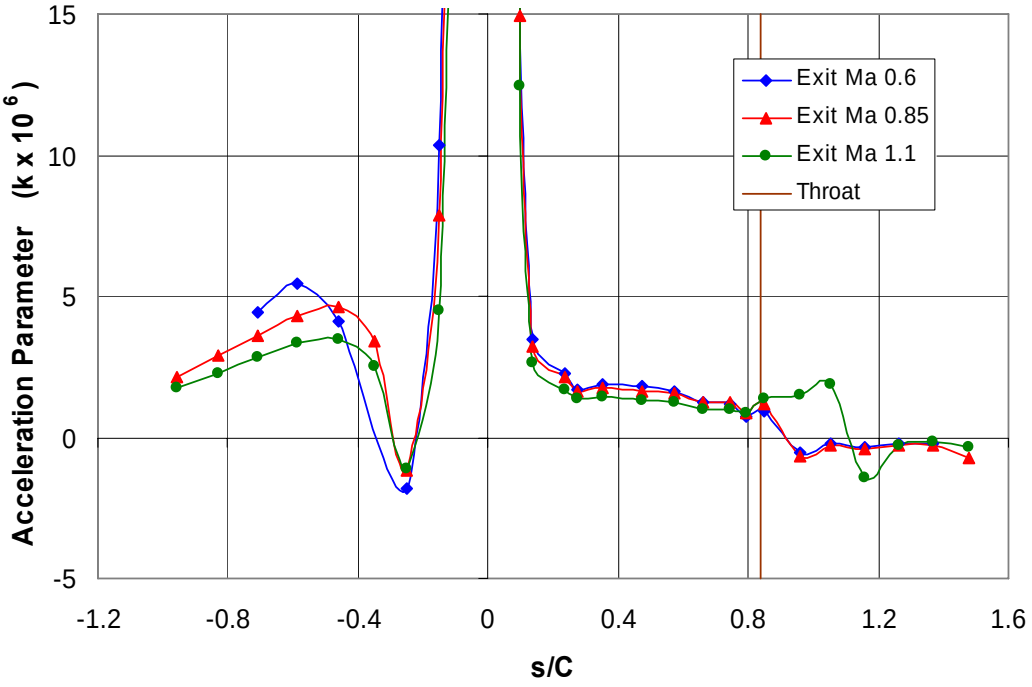

Figure B-5. Plot of the acceleration parameter on the blade at each exit Mach number

Blade Passage Periodicity

In addition to measuring the local Mach number distribution on the middle blade, the flow periodicity was checked by measuring the pressure distributions on adjacent blades with pressure taps. Due to the limited number of pressure transducers, the suction side periodicity had to be checked in a different set of tests than the pressure side periodicity. Tests were repeated several times to ensure that the experiments were repeatable. The flow on the pressure of the blades showed the same Mach number distributions on the middle and upper blades. On the suction side of the middle and lower blades, the flow exhibited the same Mach number distributions up to the throat and then slightly different Mach number distributions near the throat. This indicates that the flow is slightly nonperiodic downstream of the throat on the suction side. Figure B-6 provides the periodicity plot through the blade passages.

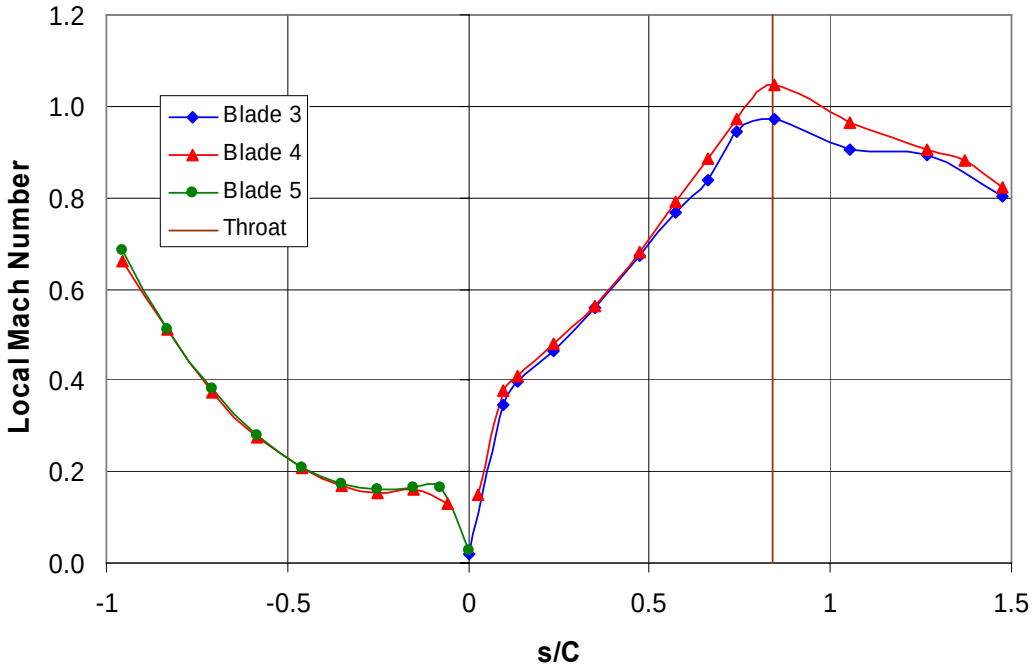

Figure B-6. Plot of the blade passage perodicity on the pressure and suction sides of the blade

Fluent Comparison

A CFD analysis of the blade aerodynamics was performed by Shakeel Nasir using Fluent. A single blade passage was meshed using Gambit and imported into Fluent. Experimental conditions were used as the inputs to the model and a one equation turbulent viscosity Spalart-Allmaras model was used. Overall, the CFD results compare well with the experimental data at exit Mach 0.85 conditions. There is good agreement between the experimental data and the CFD predictions on the pressure side of the blade. The suction side of the blade compares very well up to the throat area at which point Fluent appears to predict a shock that does not appear to be present in the experimental data. A picture of the mesh of the setup along with the CFD prediction of the Mach number distribution at exit Ma 0.85 is shown in Figure B-7. A plot of the CFD prediction of the Mach number distribution as compared to the experimental results is provided in Figure B-8. The CFD comparisons at exit Mach 0.6 and 1.1 are provided in Figures B-9 and B-10.

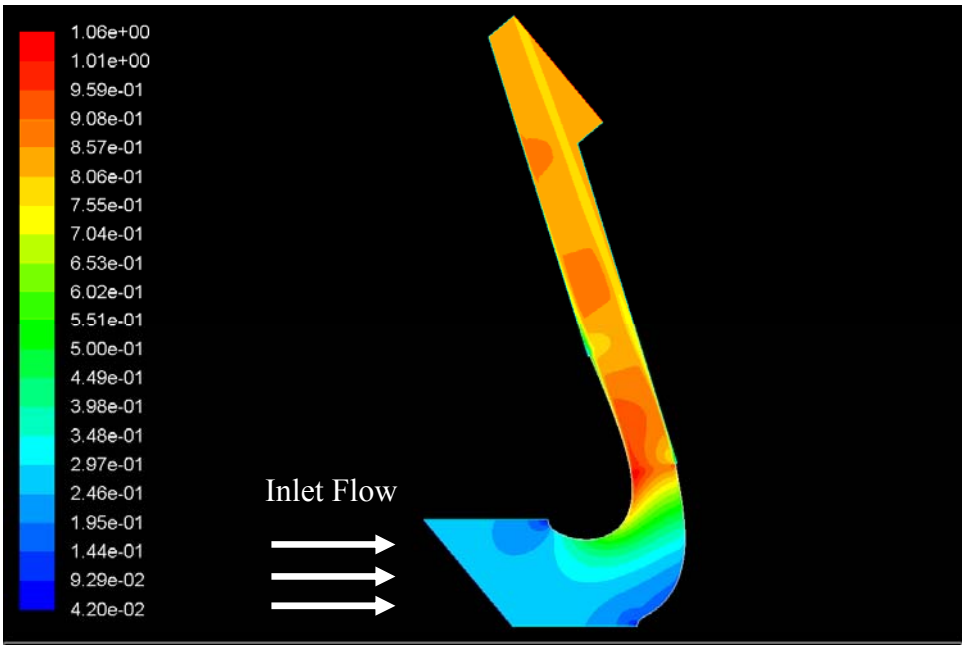

Figure B-7. Picture of the Mach number distribution in the blade passage from the Fluent output

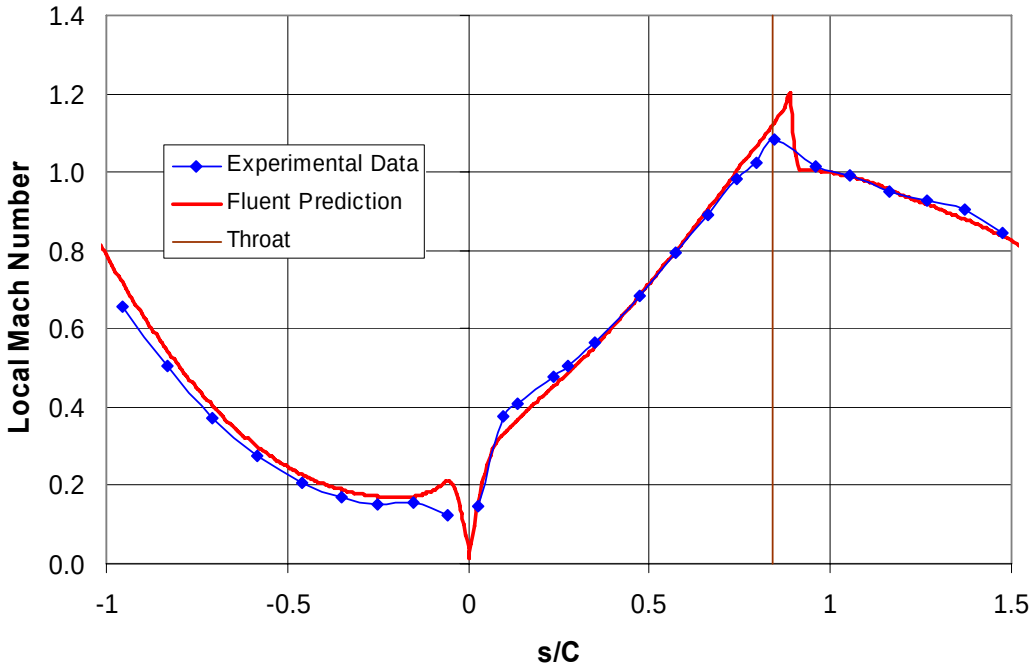

Figure B-8. Plot of the local Mach number distributions comparing the CFD prediction with the experimental results at exit Mach 0.85

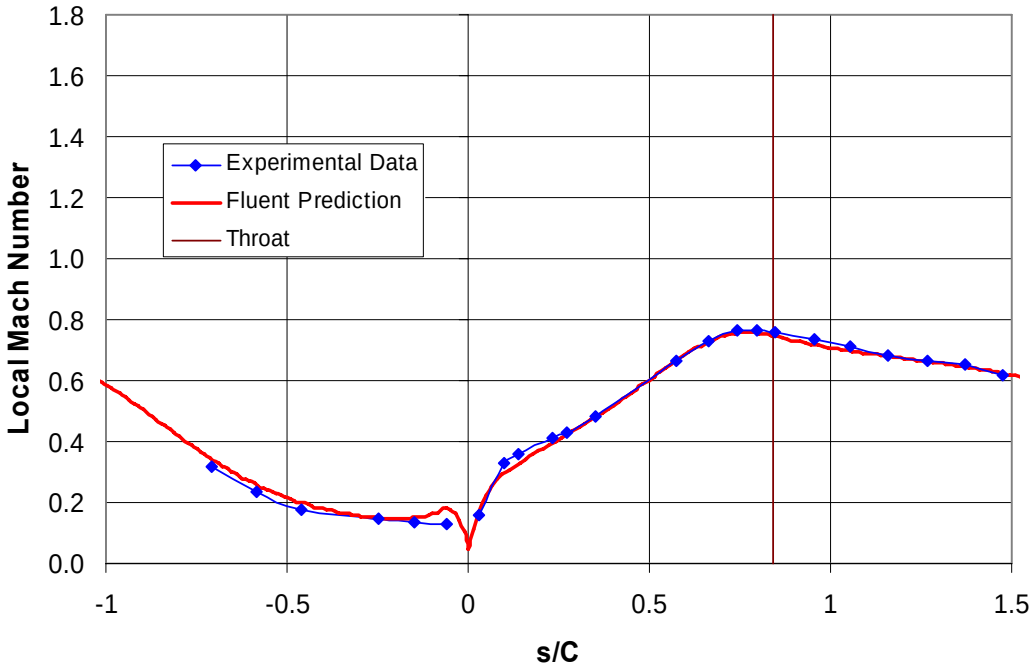

Figure B-9. Plot of the local Mach number distributions comparing the CFD prediction with the experimental results at exit Mach 0.60

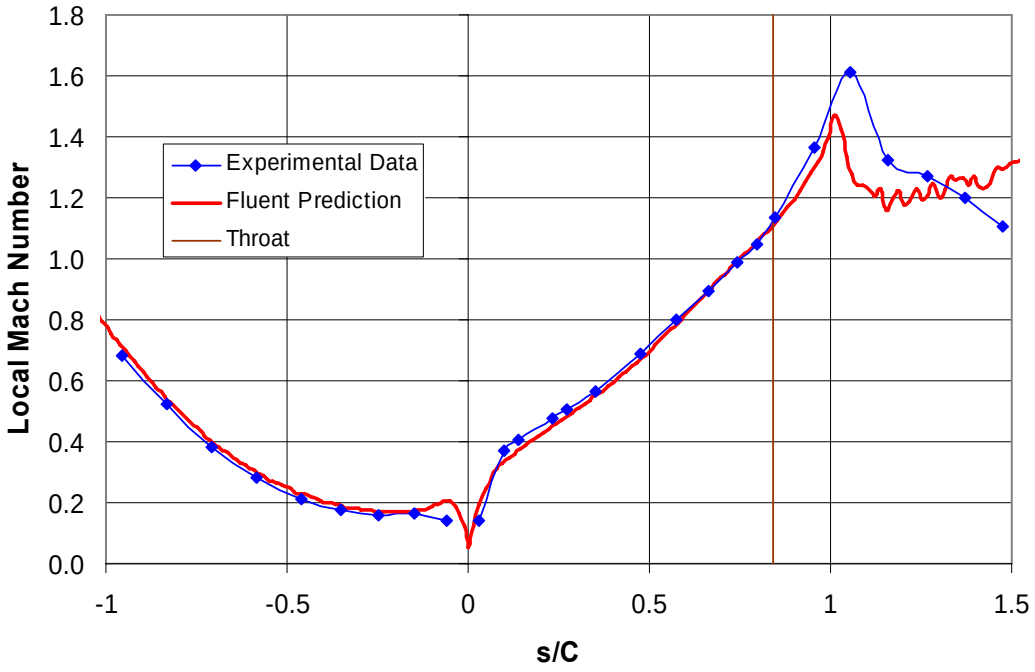

Figure B-10. Plot of the local Mach number distributions comparing the CFD prediction with the experimental results at exit Mach 1.1

Appendix C Turbulence Generation and Instrumentation

Instrumentation

Turbulence measurements were made with a single-wire hot film. The hot film probe that was used is a TSI 1201 hot film that was connected to a Dantec Type 55M01 anemometer that kept the temperature of the hot film constant by varying the voltage. For the remainder of this report, the hot film will be referred to as a hot wire since more people are familiar with hot wire probes. Hot film and hot wire probes have the same exact operating principals with the wire construction and wire size being the primary difference between the probes. A hot film has a slightly slower response time than the hot wire probe, but is more robust since it has a larger wire size. The output from the Dantec system was passed through the signal conditioner portion of the TSI IFA-100 system. The IFA-100 system performed the filtering and added a gain to the signal before the signal was recorded using a Nicolet BE256-LE system.

During hot wire calibration, the hot wire anemometer output signal was filtered at 400 Hz using the IFA-100 signal conditioner and sampled at 1000 Hz with the BE256-LE system. To make the turbulence measurements, the hot wire anemometer output signal was filtered at 40 kHz using the IFA-100 signal conditioner and sampled at 100 kHz with the BE256-LE system. The sampling time was adjusted so that the number of samples collected would equal 2^x, where x is an integer. Typically data was collected for 0.65 sec (2^{16} samples at 100 kHz) or 1.31 sec (2^{17} samples at 100 kHz). This number of samples collected was done so that the hot wire data could be properly frequency averaged.

Hot Wire Calibration

A calibration of each hot wire probe was performed prior to performing a turbulence measurement. The goal of the calibration is to correlate the voltage output of the hot wire to the velocity of the flow. The calibration of the hot wire was performed with no turbulence grid installed in the wind tunnel. This allowed for the smallest amount of velocity fluctuations in

which to calibrate the hot wire. Using a pitot static probe, the total and static pressure of the flow were measured using MKS 223B pressure transducers. An air probe type-T thermocouple was used to measure the total temperature of the flow upstream of the test section. An ice bath was used as a reference temperature for the thermocouple. The voltage output of the hot wire, pressure transducers and the thermocouple were all sampled at 1 kHz using the BE256-LE system for 60 seconds. The tunnel was run for roughly 40 seconds so that hot wire could be calibrated over a range of velocities.

The static and total pressures were used to calculate the Mach number of the flow using equation B-1. With the Mach number and the total temperature, the static temperature of the flow was determined using equation C-1,

$$T = \frac{T_0}{1 + \frac{\gamma - 1}{2} \cdot Ma^2} \tag{C-1}$$

where γ is the specific heat ratio, Ma is the Mach number of the flow and T_0 is the total temperature of the flow. The Mach number was then converted into a velocity using the temperature as shown in equation C-2,

$$U = Ma \cdot \sqrt{\gamma \cdot R \cdot T} \tag{C-2}$$

where γ is the specific heat ratio of air, R is the gas constant of air and T is the static temperature of the flow. The density of the flow was found by using the ideal gas equation as given by equation C-3,

$$\rho = \frac{p}{R \cdot T} \tag{C-3}$$

where p is the static pressure of the flow. Empirical correlations were used to estimate the dynamic viscosity as a function of temperature. With the flow data, the instantaneous Reynolds number was found using equation C-4,

$$\mathrm{Re} = \frac{\rho \cdot U \cdot d_w}{\mu} \tag{C-4}$$

where d_w is the diameter of the hot wire and μ is the dynamic viscosity.

The voltage output of the hot wire was converted into a Nusselt number by using the following steps. The mean temperature of the hot wire was calculated by using equation C-5,

$$T_m = \frac{T + T_w}{2} \tag{C-5}$$

where T is the static temperature and T_w is the hot wire temperature. The flow properties are calculated at this mean temperature. The hot wire temperature, given by equation C-6,

$$T_w = \frac{R_{op} - R_0}{R_c} \cdot 100 \tag{C-6}$$

and is a function of operating resistance, R_{op}, the hot wire probe resistance at 0°C, R_c and the change in hot wire probe resistance from 0°C to 100°C, R_0. R_c and R_0 were supplied by the hot wire manufacture and the operating resistance is set by the user. With the temperatures, probe voltage output and thermal conductivities of air, a modified Nusselt number can be calculated by using equation C-7.

$$Nu' = \frac{V^2}{k \cdot (T_m - T)} \cdot (T_m - T)^{-0.17} \tag{C-7}$$

This Nusselt number is referred to as a modified Nusselt number because it is not nondimensionalized. The thermal conductivity, k, of air was calculated using an empirical equation that is a function of temperature,

Once the Reynolds numbers and the modified Nusselt number at each measurement time, the data was plotted and an exponential curve fit was applied to the data. The curve fit is in the form of equation C-8,

$$Nu' = A \cdot \mathrm{Re}^B \tag{C-8}$$

where A and B are calibration constants. A calibration was performed for each probe. Probes were calibrated shortly before they were used to make turbulence measurements. This calibration procedure is similar to the procedure used by Nix [F.4]. A sample calibration curve is provided in Figure C-1.

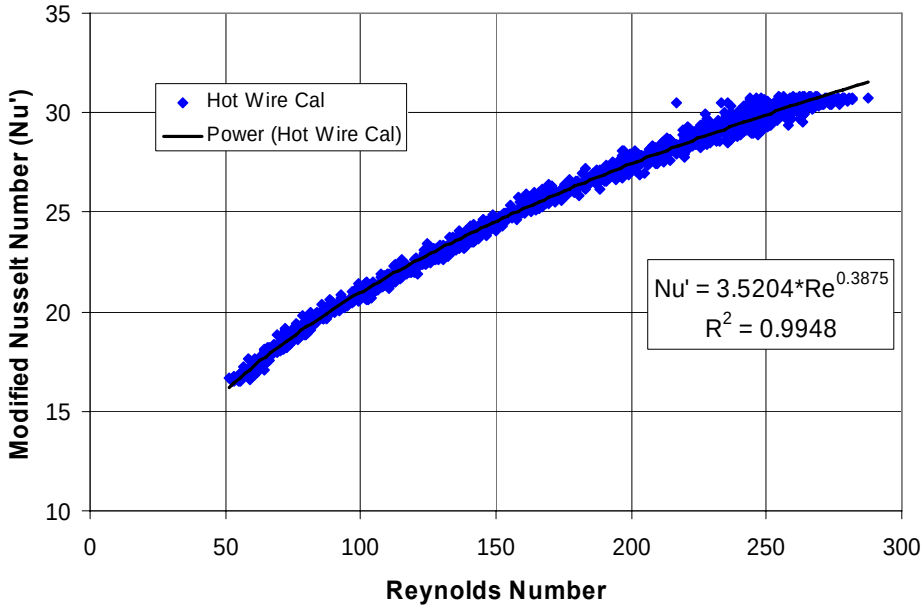

Figure C-1. Plot of the calibration curve of a hot wire

Turbulence Grids

Two passive turbulence grids were developed that would generate freestream turbulence levels between 10% and 15%. The designs of the two grids were based off of correlations developed by Baines and Peterson [F.5] and by the work of Nix et al. [F.6]. One turbulence grid was a square mesh grid and the other was a square bar grid. Multiple experiments were performed to get the desired turbulence levels with the grids. The distance between the turbulence grid and the cascade inlet was varied by adding or removing spacers. This change in distance alters the turbulence level and length scale measured at the cascade inlet. The turbulence level generated by the grid could also be adjusted by moving the grid upstream of the contraction. The turbulence level decreases as the flow goes through the contraction.

The square mesh turbulence grid was positioned downstream of the contraction with two spacers placed between the turbulence grid and the test section. The square mesh grid had bars that are 0.75 in. wide and spaced such that 1.5 in. square openings are created. There are six bars in the horizontal direction and two bars in the vertical direction. The square mesh grid created a

blockage area of 48%. Figure C-2 provides a schematic of the square mesh turbulence grid and Figure C-3 shows the grid installed in the wind tunnel.

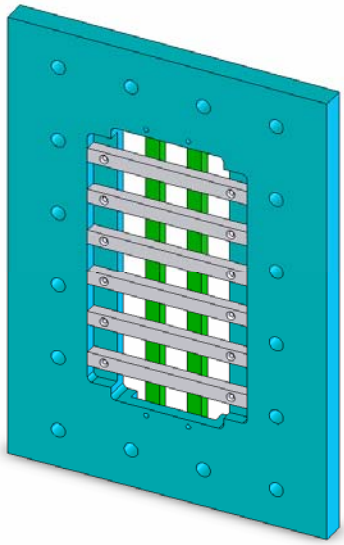

Figure C-2. Schematic of the square mesh turbulence grid

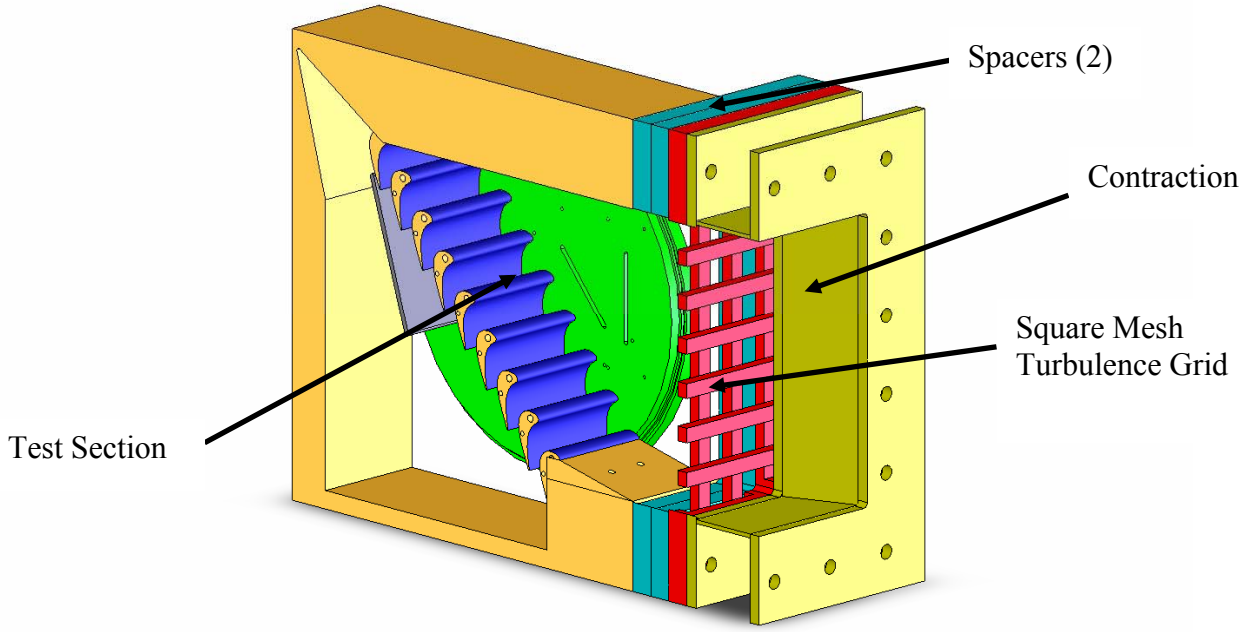

Figure C-3. Schematic showing the position of the square mesh turbulence grid relative to the test section

The second configuration is a bar turbulence grid that is positioned upstream of the contraction. Four spacers are placed between the contraction and the test section to create the desired turbulence. The bar grid had three bars that were 2.5 in. wide and spaced 1.875 in. apart.

The bars create a blockage area of 50%. Figure C-4 provides a schematic of the bar turbulence grid and Figure C-5 shows the grid installed in the wind tunnel.

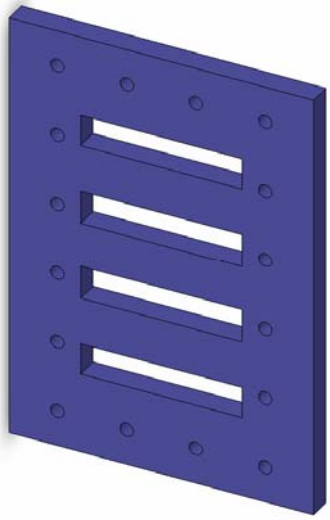

Figure C-4. Schematic of the bar turbulence grid

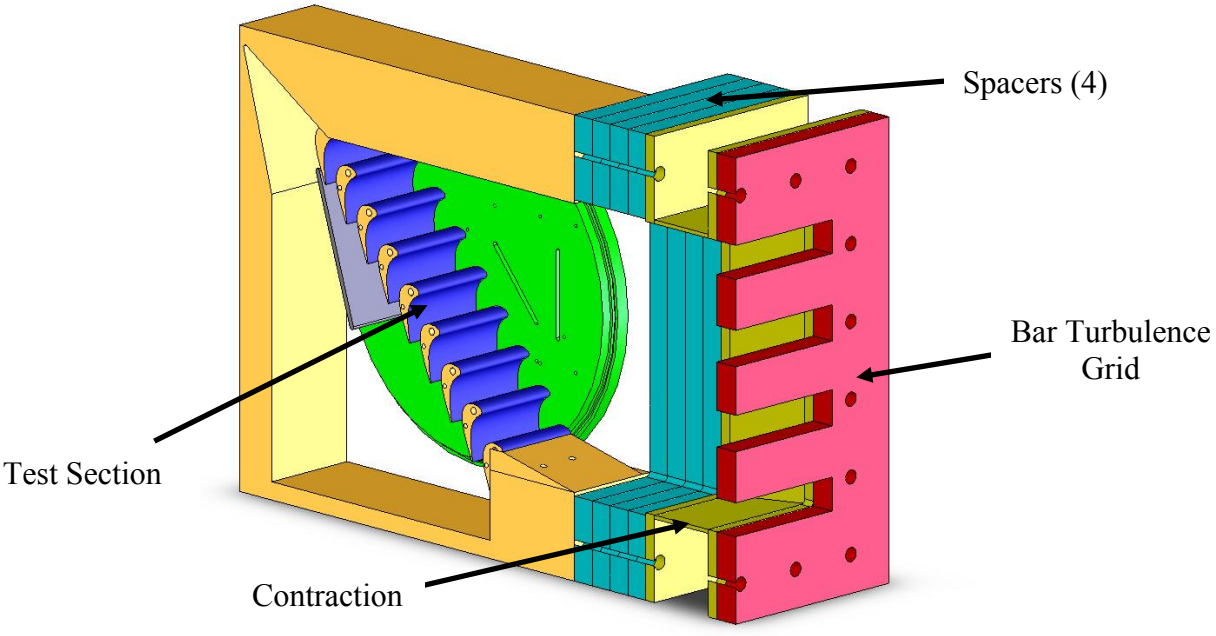

Figure C-5. Schematic showing the position of the bar turbulence grid relative to the test section

Turbulence Measurements

The turbulence generated by the grids was measured using a single wire hot film probe. The hot film measures the instantaneous velocity of the flow and from the instantaneous velocity, the freestream turbulence levels and turbulence length scales could be calculated. In a single run, the hot film probe was traversed to five discrete locations to measure the instantaneous velocity at each location. The probe traversed a full blade pitch with the center of the traverse located at the leading edge of the middle blade. Measurements are made in the two slots upstream of the blade passage. The slot closest to the blade passage is parallel to the blade inlet and spaced 0.6 chords upstream of the blades. The slot furthest to the blades is perpendicular to the flow and spaced 1.8 chords upstream of the leading edge of the middle blade. The locations of the slots relative to the blades are shown in Figure C-6.

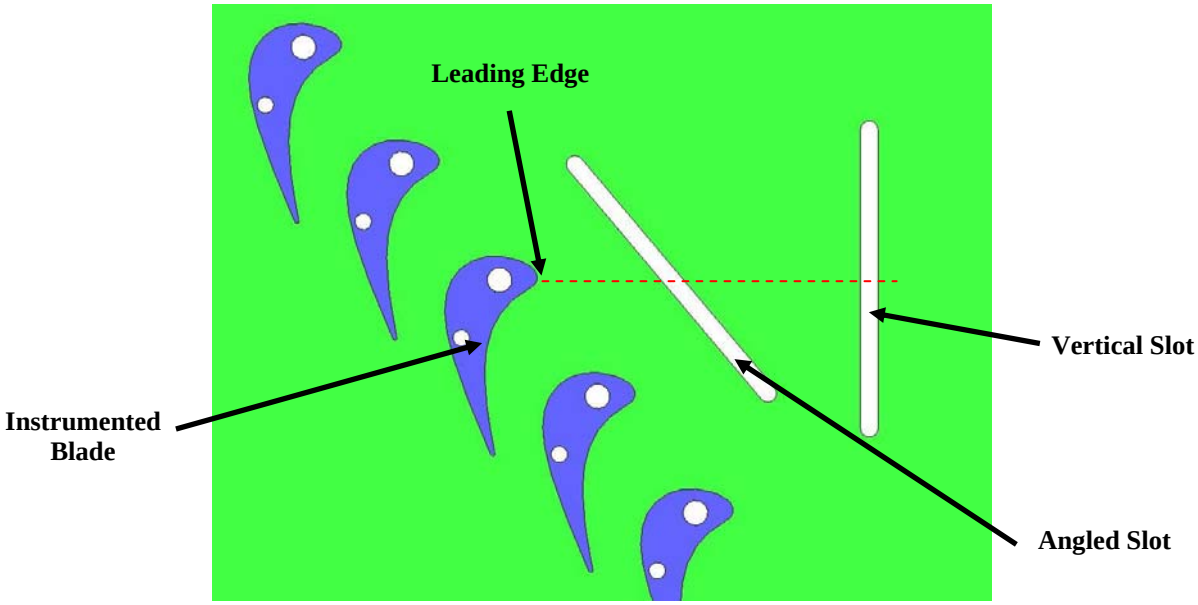

Figure C-6. Schematic showing the location of the measurement slots in the test section

After making the measurements with the hot wire, the voltage signal was converted into an instantaneous velocity by applying the calibration. The methologogy presented here is the same procedure that was used by Nix [F.4] and Sauer [F.7]. With the instantaneous velocity, the mean velocity could be calculated using equation C-9,

$$U_{Mean} = \frac{1}{n} \cdot \sum_{i=1}^{n} U_i \qquad \text{(C-9)}$$

where n is the number of samples and U_i is the instantaneous velocity. The average velocity fluctuations were then calculated by finding the root mean squared velocity given by equation C-10.

$$U_{RMS} = \sqrt{\frac{1}{n} \cdot \sum_{i=1}^{n} \left(U_i - U_{Mean}\right)^2} \tag{C-10}$$

With the mean velocity and the root mean squared velocity, the turbulence intensity could be calculated with equation C-11.

$$Tu = \frac{U_{RMS}}{U_{Mean}} \cdot 100 \tag{C-11}$$

A sample instantaneous velocity measurement is provided in Figure C-7 and the corresponding velocity histogram is show in Figure C-8.

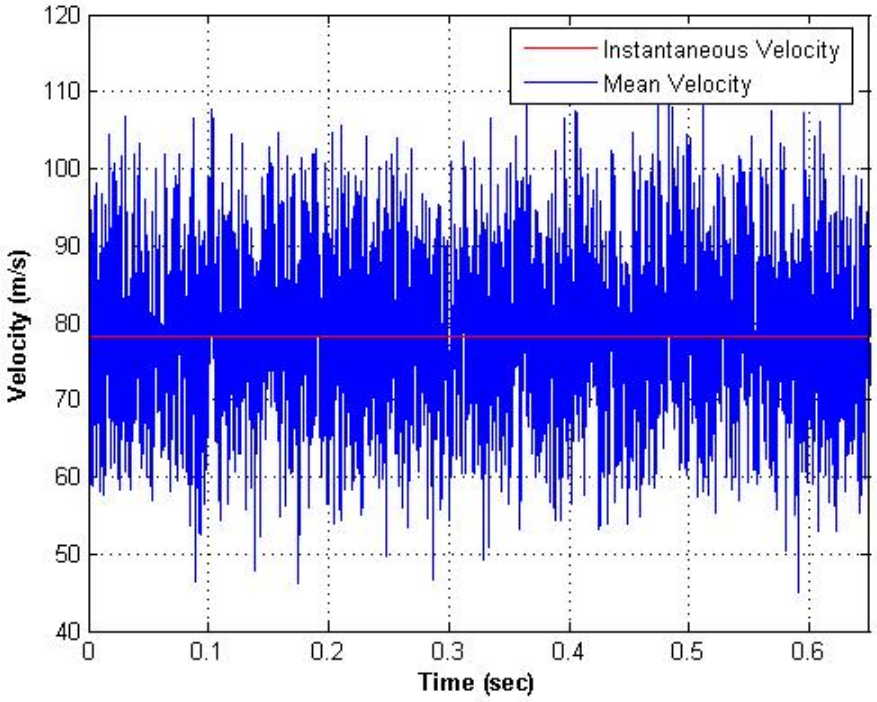

Figure C-7. Plot of the instantaneous velocity versus time measured by the hot wire

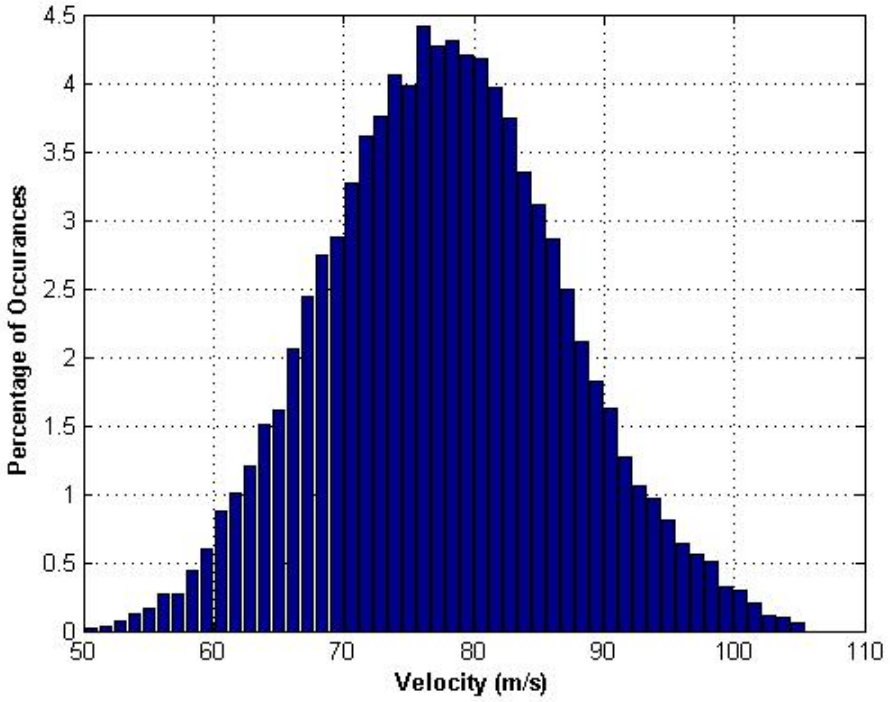

Figure C-8. Plot of the velocity histogram of the flow

The flow was also analyzed when by looking at the power spectral density. The power spectral density shows the frequency content of the turbulence. Basically, the power spectral density indicates what frequencies are occurring most often in the flow and the energy that is contained at that frequency. The power spectral density was calculated by breaking the total number of samples into equal parts and performing a fast Fourier transform (FFT) on each part of the total signal using the FFT function (fft) in Matlab. The FFT on each part of the signal was then averaged to get the average FFT. The FFT is divided by the frequency resolution to get the power spectral density.

The power spectral density was then normalized and compared to the theoretical Von Karman spectrum. The Von Karman spectrum is a theoretical spectrum when the turbulence is isotropic. The Von Karman relation for isotropic turbulence as reported by Hinze [F.8] and Nix [F.4] is provided by equation C-12,

$$\frac{E(f)\cdot U_{Mean}}{{U_{RMS}}^2\cdot \Lambda_x} = 4\cdot\left(1+\left(\frac{8\pi f\cdot\Lambda_x}{3\cdot U_{Mean}}\right)^2\right)^{-\frac{5}{6}} = 4\cdot\left(1+\left(\frac{\kappa}{\kappa_e}\right)^2\right)^{-\frac{5}{6}} \qquad \text{(C-12)}$$

where E(f) is the power spectral density, f is the frequency, Λ_x is the turbulence length scale, κ is the wave number and κ_e is the most energetic wave number. The wave number and the most energetic wave number are provided in equations C-13 and C-14, respectively.

$$\kappa = \frac{2\pi f}{U_{Mean}} \tag{C-13}$$

$$\kappa_e = \frac{3}{4 \cdot \Lambda_x} \tag{C-14}$$

A plot of the normalized power spectral density compared to the Von Karman spectrum is provided in Figure C-9.

The normalized power spectral density compares very well to the theoretical Von Karman spectrum. Both spectrums begin to roll off at the same frequency and heave a very similar slope. Isotropic turbulence should have a slope of -5/3. This indicates that the flow generated by this particular turbulence grid is isotropic. The two spikes in the signal are present for each turbulence measurement and occur at the same frequency in each run. These spikes are not caused by the flow but rather the anemometer or the hot wire probe.

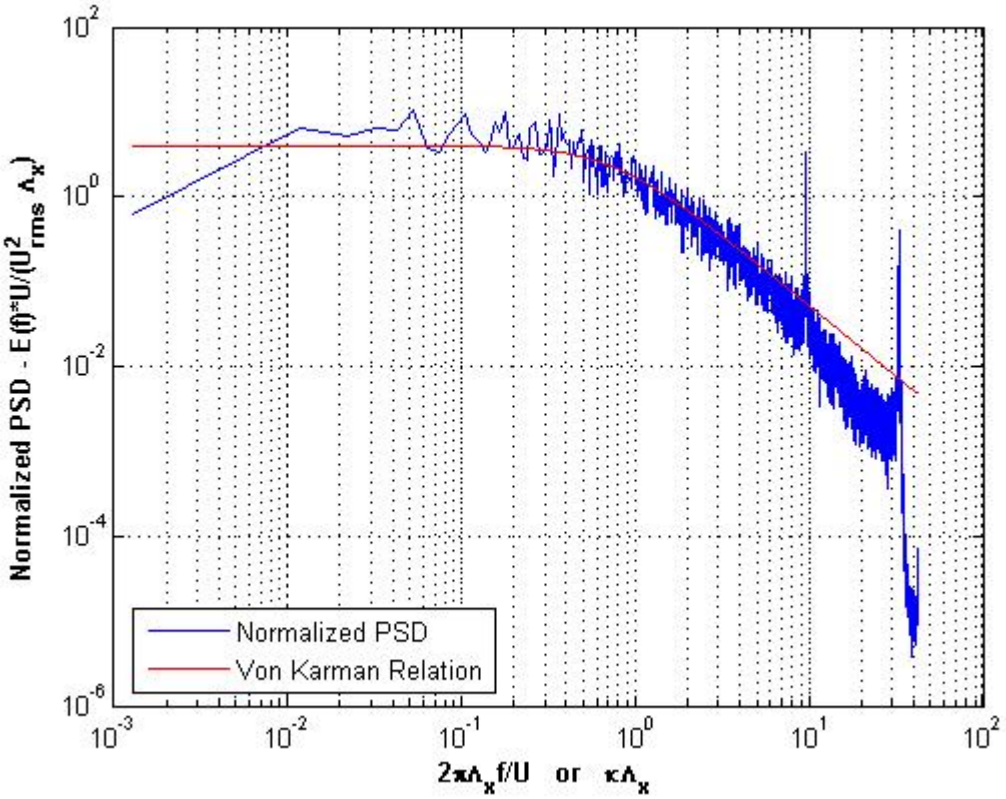

Figure C-9. Plot of the normalized power spectral density

In addition to capturing the freestream turbulence, the turbulence length scale was also calculated. The turbulence length scale is the diameter of the largest turbulent eddy. The first step in calculating the turbulence length scale was to perform the autocorrelation on the velocity signal measured by the hot wire, which is given by equation C-15,

$$R_{11} = \frac{\sum_{i=1}^{n-x} \left(U_i - U_{Mean}\right) \cdot \left(U_{i+x} - U_{Mean}\right)}{\sum_{i=1}^{n} \left(U_i - U_{Mean}\right)^2} \qquad \text{(C-15)}$$

The autocorrelation function (xcorr) in Matlab was used to perform the autocorrelation on the signal. The autocorrelation function was normalized so that when the signal was completely correlated at zero lag time would be equal to one. When the normalized autocorrelation value was equal to zero, the signals were no longer correlated. A plot of the autocorrelation is provided in Figure C-10.

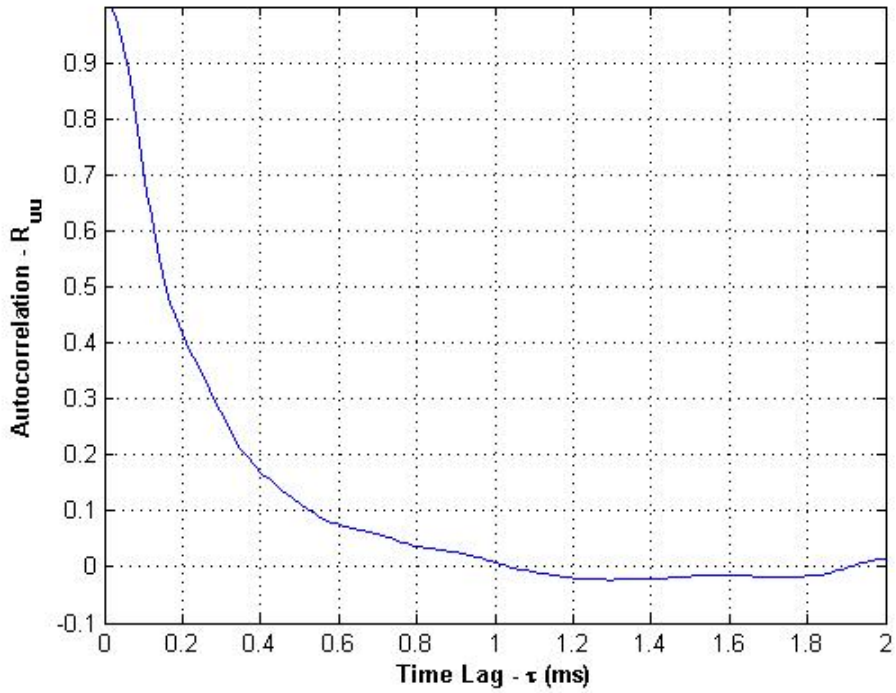

Figure C-10. Plot of the autocorrelation for the hot wire signal

The area under the autocorrelation curve was found from the zero lag time to the first zero crossing by using equation C-16,

$$T = \sum_{i=1} R_{11i} \cdot \Delta\tau \tag{C-16}$$

were $\Delta\tau$ is the time between the discrete points. The area under the autocorrelation curve is the integral time scale. With the integral time scale determined, the integral turbulence length scale could be determined by using Taylor's Hypothesis of frozen turbulence given by equation C-17,

$$\Lambda_x = U_{Mean} \cdot T \tag{C-17}$$

To normalize the turbulence length scale, the length scale was divided by the pitch of the blade. The methods of calculating the turbulence level and the integral length scale were used in the analysis of each turbulence grid.

Turbulence Results

Turbulence measurements were made with the hot wire probe on the turbulence grids are summarized in this section. In the angled slot, the turbulence levels and length scales varied somewhat across the inlet pitch. This variation is due to each measurement location being a different distances from the turbulence grid. For example, the point y/P = -0.52 is closest to the turbulence grid and the point y/P = 0.52 is the furthest from the turbulence grid. Measurement locations closer to the grid have higher turbulence intensities since the turbulent eddy dissipates as the eddy moves further downstream from the grid. The turbulence intensity and length scale variations along the inlet pitch for the baseline, square mesh grid and the bar grid are provided in Figures C-11 and C-12.

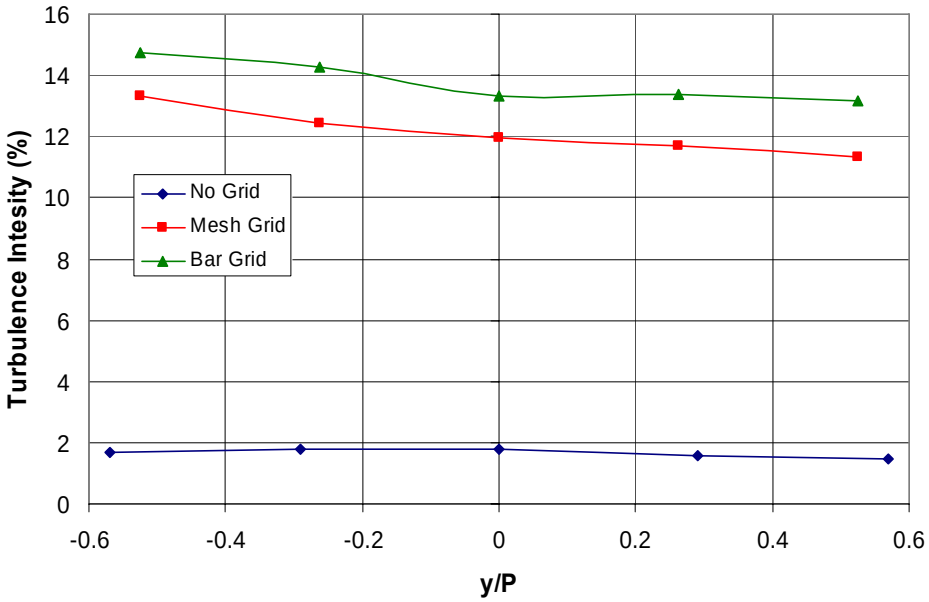

Figure C-11. Plot of the turbulence intensity across the angled slot

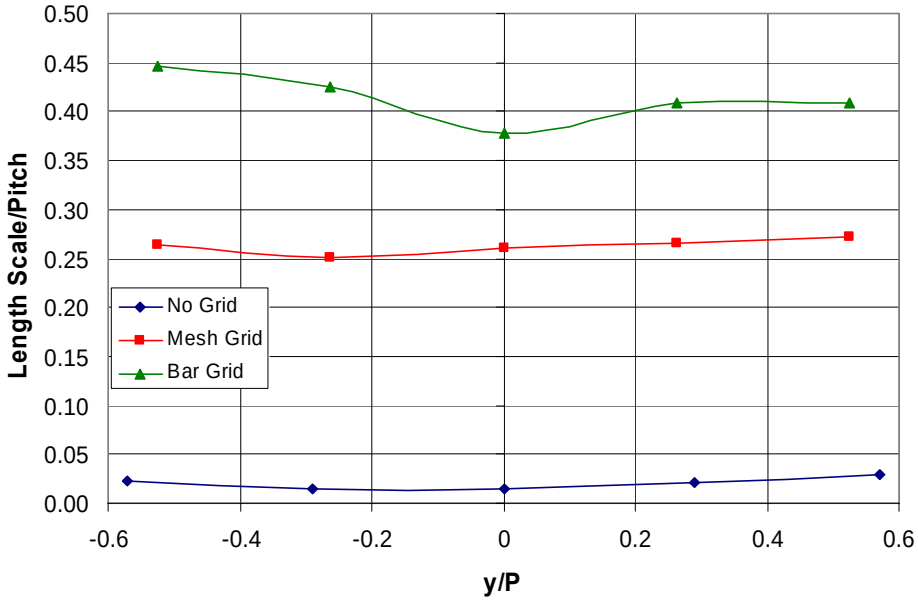

Figure C-12. Plot of the normalized turbulence length scale in the angled slot

The turbulence levels in the vertical slot were also measured at discrete locations. Since the distance between the measurement locations in the vertical slot is constant, any variation in the turbulence level would be due to the turbulence being nonuniform.

Since there is some variation in the turbulence level and length scale across the inlet pitch, the turbulence levels and lengths scales were averaged. The baseline case with no turbulence grid has a turbulence intensity of 1.7% and a nondimensional length scale of 0.02. The square mesh grid generates a turbulence intensity of 12.2% and a nondimensional length scale of 0.26. The bar grid produces a turbulence intensity of 13.8% and a nondimensional length scale of 0.41. The turbulence and length scale data is summarized in Table C-1.

Table C-1. Summary of the turbulence intensity and turbulence length scale measured in the angled slot

	Turbulence Intensity (%)	Length Scale (cm)	Length Scale/ Pitch (Λ_x/P)
Baseline	1.7	0.12 cm	0.02
Mesh Grid	12.2	1.52 cm	0.26
Bar Grid	13.8	2.40 cm	0.41

From the measurements in the angled and vertical slots, decay curves could be created for each turbulence grid. The turbulence decay curves from both grids were compared to the decay correlations for isotropic turbulence from Baines and Peterson [F.5] and Roach [F.9] given by equation C-18,

$$Tu = 1.13 \cdot \left(\frac{x}{B} \right)^{-\frac{5}{7}} \qquad \text{(C-18)}$$

where x is the distance downstream from the grid and B is the bar size. This correlation is based on empirical data. The turbulence intensity decreases because of viscous dissipation effects on the turbulence eddy. The turbulence decay curves for both turbulence grids fall below the correlation decay curves, but follow the same trends as the correlation. The turbulence levels being below the correlations were also observed by Nix et al. [F.4] in the transonic cascade facility. A plot of the turbulence decay is provided in Figure C-13.

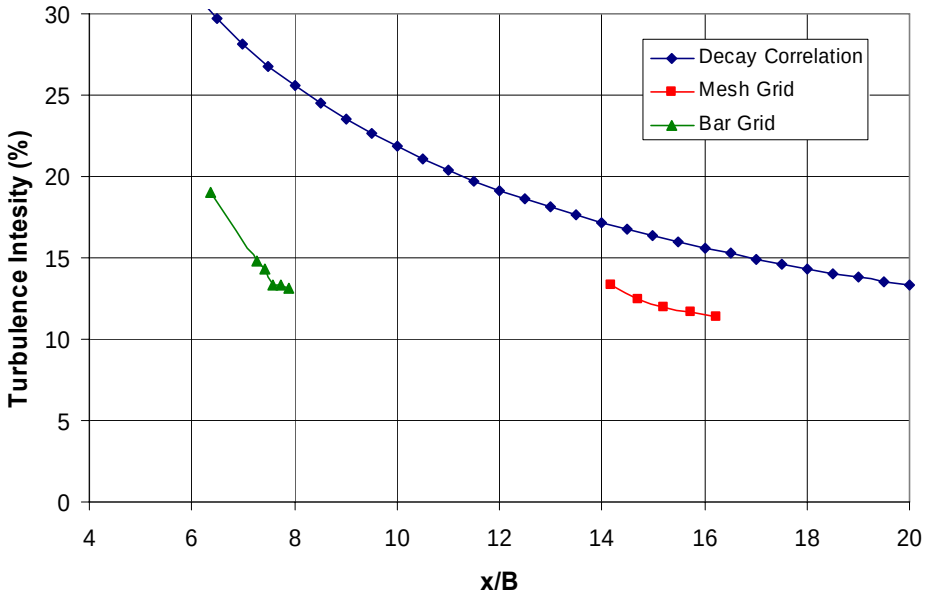

Figure C-13. Plot of the turbulence decay

The size of the turbulence length scale was also compared to the correlations reported in literature. The turbulence length scale will increase in diameter as the turbulent eddy flows downstream from the turbulence grid. The increase in eddy size is caused by inertial effects on the turbulent eddy. The turbulence length scale for isotropic turbulence increases in size according to equation C-19,

$$\frac{\Lambda_x}{B} = 0.2 \cdot \left(\frac{x}{B} \right)^{\frac{1}{2}} \qquad \text{(C-19)}$$

as reported by Baines and Peterson [F.5] and Roach [F.9]. The measured turbulence length scales for the square mesh grid lie right on top of the empirical correlation and displays the same trend. The length scales for the bar grid are slightly below the correlation. This is most likely due to the flow passing through the contraction. A contraction will typically decrease the turbulence level and decrease the size of the turbulent eddies of a flow. A plot of the length scale increase is provided in Figure C-14.

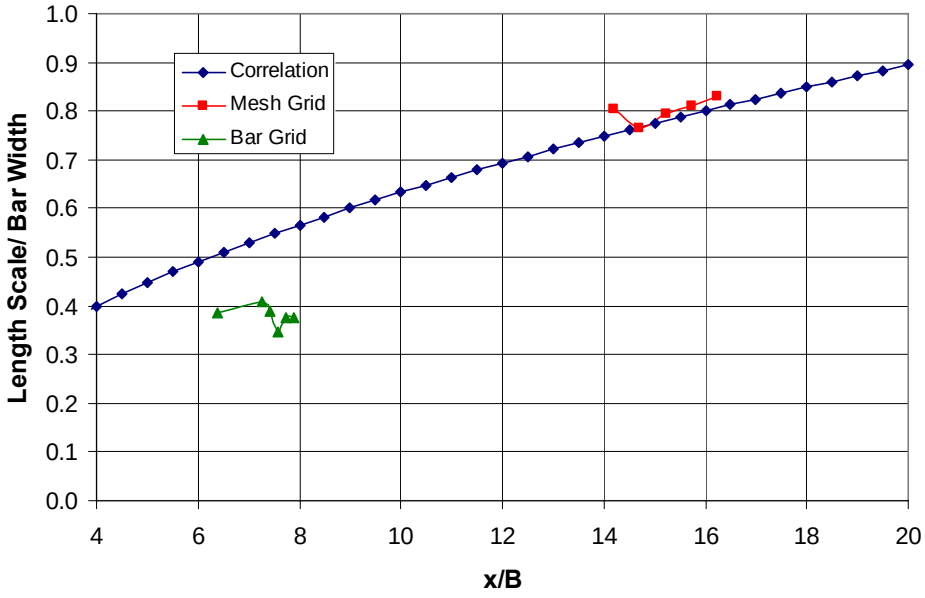

Figure C-14. Plot of the turbulence length scale increase in size

Inlet Velocity Uniformity

In addition to checking the turbulence levels at the inlet of the blade cascade, the inlet velocity uniformity was also measured. This measurement was performed to ensure that the flow downstream of the turbulence grid was uniform when the flow entered the cascade. The inlet velocity uniformity was measured by traversing a Kiel probe in the slots upstream of the blade passages. The Kiel probe measured the total pressure and was continuously traversed at a slow speed. A stationary Pitot static probe was also used to measure the total and static pressures of the flow. Using the total and static pressures, a pressure ratio was calculated for both the Kiel and Pitot probes. The pressure ratios were then converted to a Mach number by using equation B-1. A velocity ratio (Mach number ratio) of the Kiel probe velocity to the Pitot probe velocity was then calculated. The baseline case showed very little velocity fluctuation. The 2.5" bar grid had the largest variation in inlet velocity out of the three cases. Figure C-15 provides the plot of the velocity ratio for the three cases along the inlet pitch.

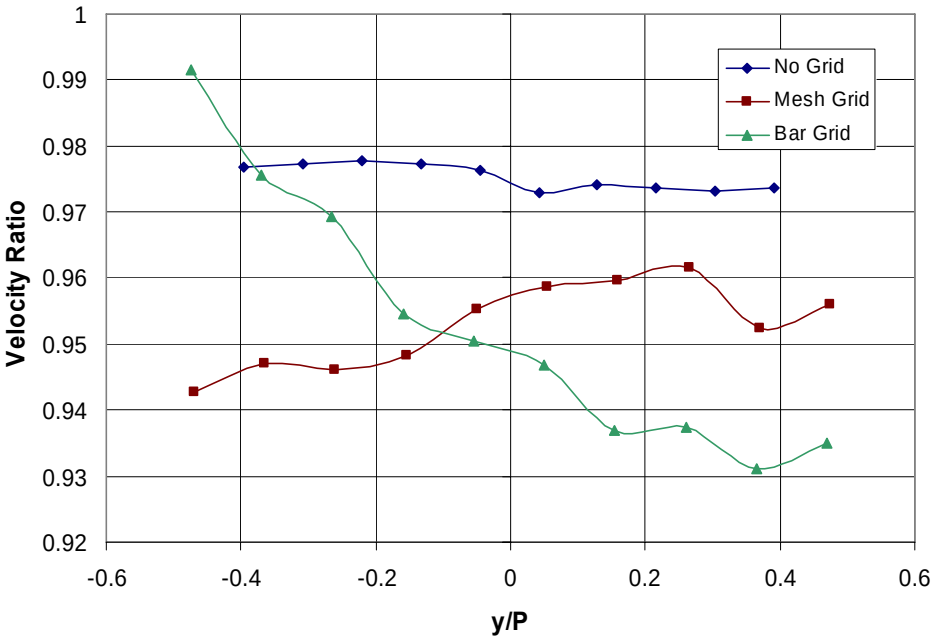

Figure C-15. Plot of the velocity ratio along the inlet pitch

Appendix D Thin Film Gauge Overview

Thin Film Gauges

The thin film gauges were used to determine the heat transfer to the turbine blade. Thin film gauge measurement technique was originally developed at Oxford University by the work of Schultz and Jones [F.10]. The thin film gauges have changed somewhat since their initial development, but the operating principles have remained the same. The thin film gauges used in these experiments are based off of the work of Joe [F.11] and manufactured at the Air Force Research Laboratory at Wright-Patterson AFB. Additional descriptions of thin film gauge operation can be found in Doorly and Oldfield [F.12] and Dunn [F.13].

A thin film gauge consists of a small platinum wire that changes resistance with temperature. Each end of the platinum is connected to copper leads. Gauges are connected to a Kapton sheet through a sputtering process. A typical Kapton sheet would have up to 25 gauges sputtered onto the sheet. The Kapton sheet attaches to the blade with thin layer of adhesive. The turbine blade instrumented with thin film gauges is a low thermal conductivity ceramic called Macor. The low thermal conductivity Macor allows for a longer test time since the conduction rate through the blade is slower as compared to a blade machined from aluminum. A total of 36 thin film gauges were installed on the turbine blade. A picture showing the thin film gauges installed on the blade is provided in Figure D-1.

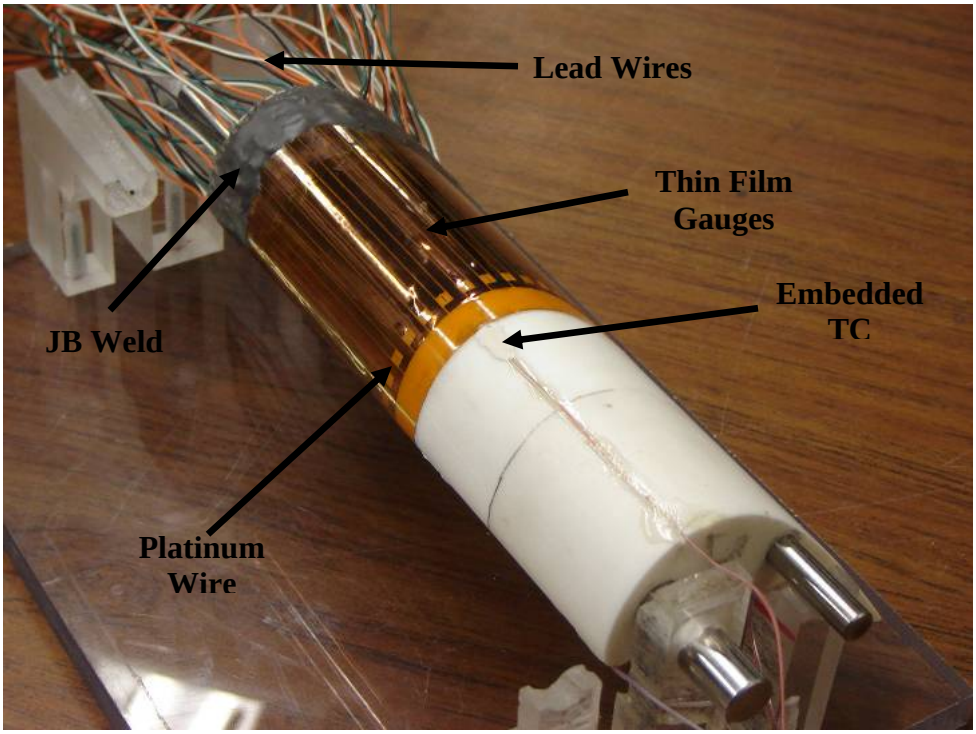

Figure D-1. Picture showing the blade with the thin film gauges installed

Once the gauges were installed on the Macor blade, the lead wires were soldered to the copper leads. The resistance of each gauge was measured and recorded after soldering of the lead wires. A layer of JB Weld was applied over all of the solder joints to make sure that the lead wires would not detach from the gauges due to the high speed flow during a test run. The JB Weld is nonconductive and does effect the operation of the gauge. Next, the gauges were placed in an oven and the gauges are heated up to 85°C. The gauges were held at this elevated temperature for about 2 hours so that the blade could reach a constant temperature. The gauge resistance at an elevated temperature was measured and recorded. The blade was allowed to cool back down to ambient temperature and the resistance of each gauge was again recorded. This process was performed to ensue that each gauge was working properly.

After checking to see that each gauge was working properly, the gauges were calibrated over the range of temperatures that the gauges will experience during an experiment by using a low temperature incubator. The calibration consisted of increasing the temperature of the incubator in discrete steps from ambient up to ~55°C and recording the resistance of each gauge at that temperature. The temperature of the incubator was then decreased back to ambient in discrete steps and again the resistance of each gauge was recorded at each temperature. Typically 3 hours was allowed to pass between calibration points so that the incubator could

reach a steady temperature and to ensure that the blade was thermally soaked. Calibration points were recorded as the temperature increased and decreased to check for gauge hysteresis. Calibration curves were generated by plotting the resistance versus temperature for each gauge and then linearly curve fitting the data. There is a linear relationship between the temperature and the resistance of the gauges. A calibration curve for two of the gauges is provided in Figure D-2.

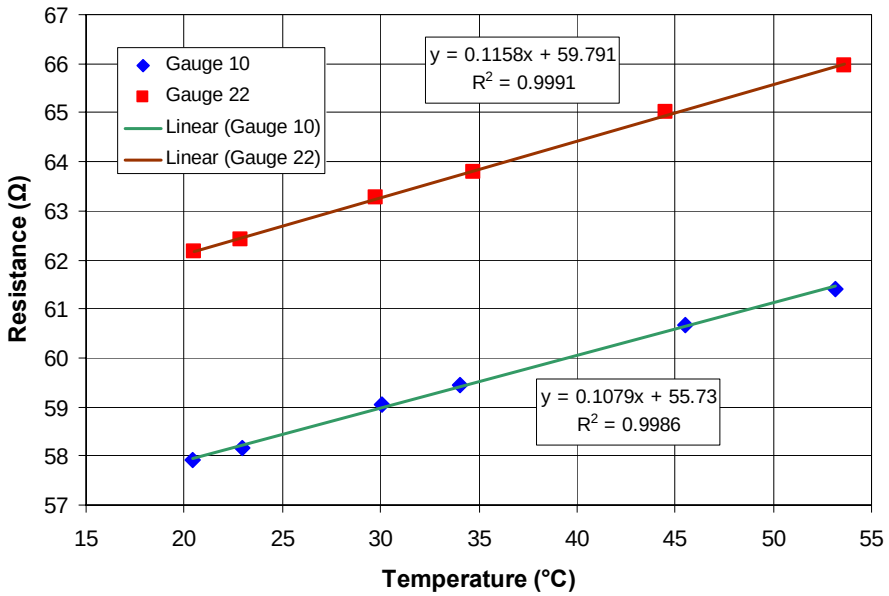

Figure D-2. Calibration curve for two of the thin film gauges installed on the turbine blade

Each thin film gauge is connected to a Wheatstone bridge circuit with the thin film gauge making one arm of the Wheatstone bridge. A DC power supply applies 10V across the circuit. The output bridge voltage is measured using National Instruments (NI) data acquisition hardware. Prior to testing the bridge is balanced using a potentiometer. As the gauge changes resistance due to temperature changes during a test run, the bridge becomes unbalanced and a change in voltage across the bridge is recorded. Figure D-3 provides a schematic of the Wheatstone bridge circuit of the thin film gauges.

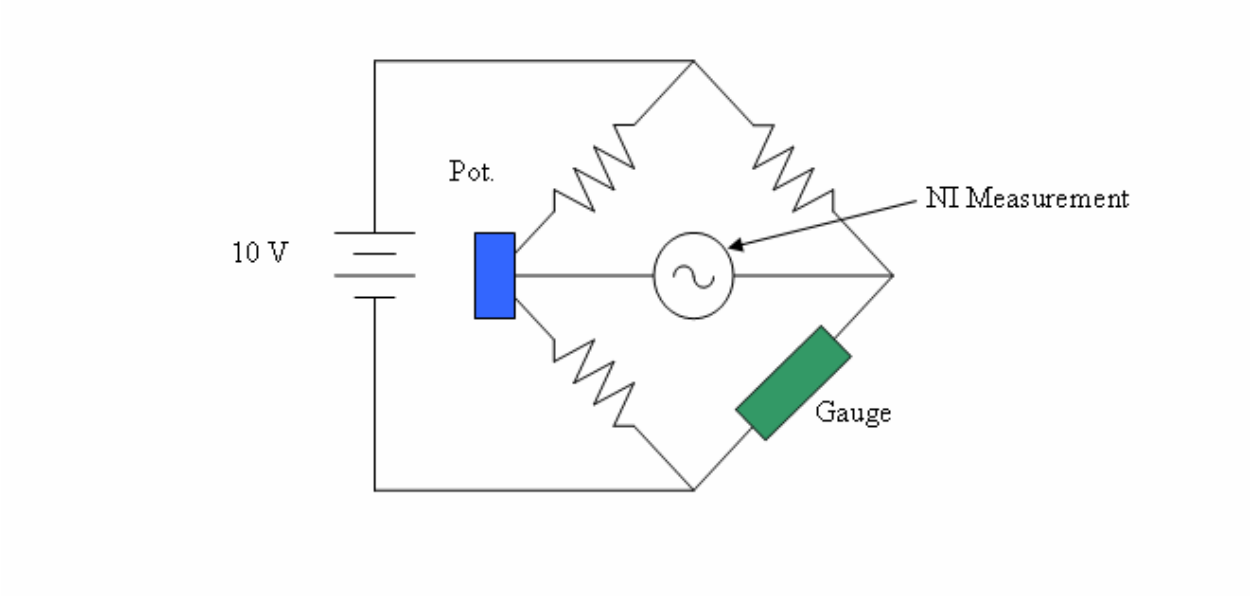

Figure D-3. Schematic of the Wheatstone bridge circuit for the thin film gauges

Data Collection

For the heat transfer experiments, three systems were used to collect data simultaneously. One NI system was used to record the voltage outputs from the Wheatstone bridges, another NI system recorded the temperatures and the PSI 8400 system recorded pressure data. Each system was triggered and recorded by a LabView 7.0 program.

The Wheatstone bridge voltage was recorded using NI data acquisition hardware that consisted of a SCXI-1001 chassis that had four SCXI-1120 isolation amplifiers connected into it. Every isolation amplifier was set to filter the signal at 10 kHz and apply a gain of 500. Each isolation amplifier was connected to a Wheatstone bridge through a SCXI-1320 terminal block. A total of 31 Wheatstone bridges were connected to the NI system. The isolation amplifiers were also connected to an SCXI-1600 16-bit data acquisition card. A USB cable was used to connect the data acquisition card to the computer. The voltage signal from the Wheatstone bridges were sampled at 1 kHz for 30 seconds to ensure that the entire run was recorded.

The temperature data was recorded with a NI SCB-68 data acquisition card. This card recorded the air temperature of the flow upstream of the test section along with the surface temperature of the blade throughout the run. The cold junction compensation internal to the data

acquisition card was used for each thermocouple. The thermocouple voltages were recorded at 1 kHz for 30 seconds.

The pressure data was recorded with the PSI 8400 system. The static pressures on the suction and pressure surfaces of blades 3 and 5 were recorded along with the total pressure upstream and several exit taps. The pressure data was sampled at 20 Hz for 30 seconds.

Heat Transfer Data Reduction

The output from the thin film gauges from the Wheatstone bridge comes in the form of a voltage versus time. The signal is converted from voltage to temperature by using the calibration constants of the gauge and basic Wheatstone bridge operating principles. Once the signal is converted into temperature, the heat flux is then calculated by using either a finite difference code or a Laplace domain code. The finite difference code assumes that the heat conduction through the blade is 1-D. The Laplace domain code assumes that the heat conduction through the blade is 1-D and semi-infinite. Because the Laplace code assumes that the heat transfer through the blade is semi-infinite, the Laplace code cannot be used at the trailing edge region. Descriptions and validations of the Laplace and finite difference codes are provided by Cress (2006). The Laplace code developed by Cress [F.14] was adapted from the work of Joe [F.11]. After the heat flux is calculated, the heat transfer coefficient is calculated using equation D-1,

$$h = \frac{q''}{\left(T_{AW} - T_{gauge}\right)} \tag{D-1}$$

where q" is the heat flux, T_{gauge} is the gauge temperature and T_{aw} is the adiabatic wall temperature. The adiabatic wall temperature is provided by equation D-2,

$$T_{AW} = T_o \cdot \left(\frac{1 + r_c \cdot \frac{\gamma - 1}{2} Ma^2}{1 + \frac{\gamma - 1}{2} Ma^2} \right) \tag{D-2}$$

where T_o is the total temperature of the air, r_c is the recover factor and Ma is the local Mach number. It was assumed that the boundary layer was turbulent everywhere, so a recovery factor of 0.892 ($r_c = Pr^{1/3}$) was applied to all of the gauges. After calculating the heat transfer coefficient, the Nusselt number is calculated by using equation D-3,

$$Nu = \frac{h \cdot C}{k} \tag{D-3}$$

where k is the thermal conductivity of the air and C is the true chord of the blade. Figure D-4 shows the progression of the heat transfer data reduction from voltage versus time to Nusselt number versus time. The Matlab code used to make these calculations is provided in Appendix G.

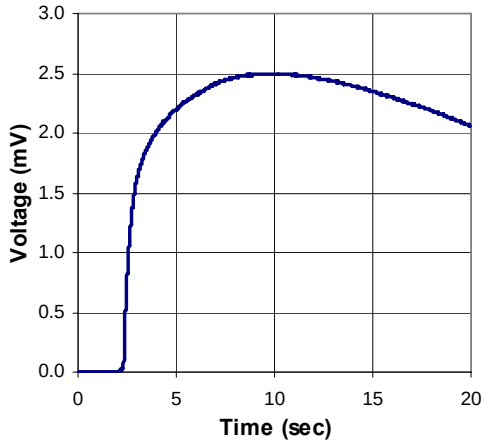

(a)

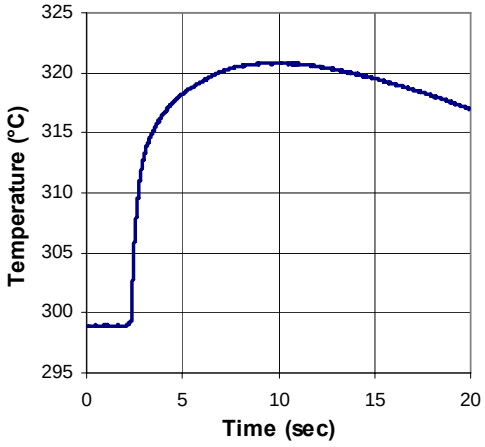

(b)

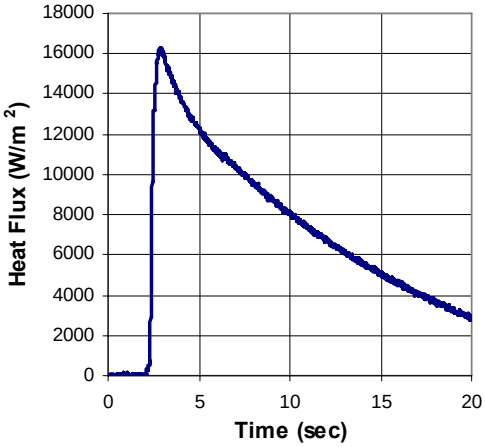

(c)

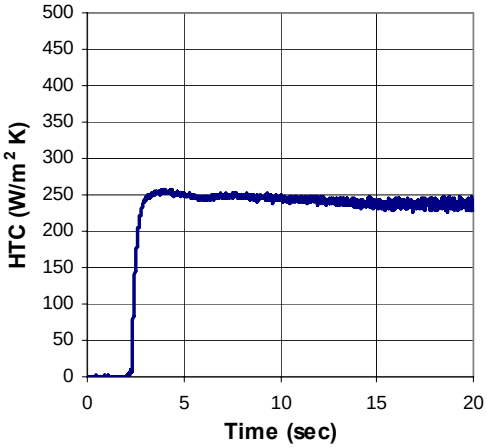

(d)

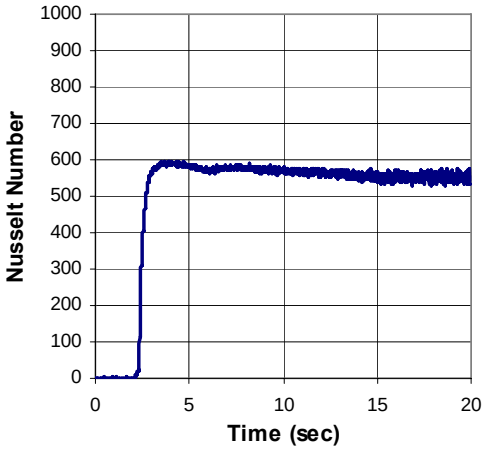

(e)

Figure D-4. Progression of the data reduction going from (a) voltage versus time, (b) temperature versus time, (c) heat flux versus time, (d) heat transfer coefficient versus time and (e) Nusselt number versus time

After calculating the Nusselt number versus time for each gauge, the data needs to be averaged to get a single Nusselt number value for a gauge. The time when the flow conditions first reached the objective exit Mach number was chosen as the time to average the data. The averaging time is in the transient region of the tunnel test run. For most of the gauges, the averaging time chosen did not have an effect on the Nusselt number, since the Nusselt number was constant versus time as shown in Figure D-4e. Only the gauges at the trailing edge of the blade had an unsteady Nusselt number. Since the trailing edge has a small material thickness (low thermal mass), all of the material at the trailing edge heats up quickly to a temperature near the blade temperature. Once the material heats up, there is a very small temperature gradient between the surface and the interior of the trailing edge. If there is no temperature difference, then there is no heat flux and those gauges can not be used. However, in the transient region of the test, the temperature gradient at the trailing edge was large enough to accurately calculate the heat flux and Nusselt number. Figure D-5 shows the location of the run where the data average occurs.

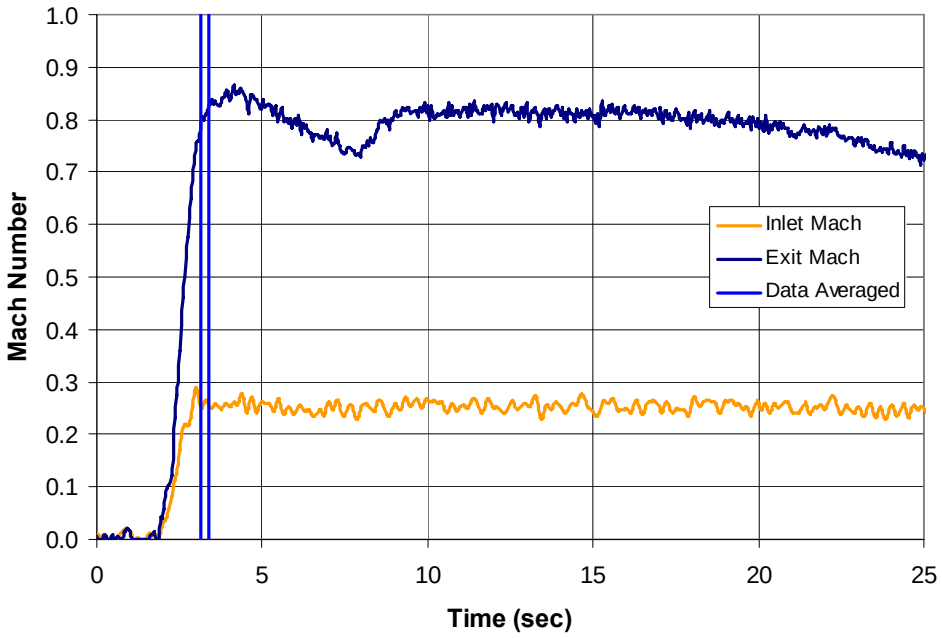

Figure D-5. Plot of inlet and exit Mach numbers for a test run showing the time where the data is averaged

Appendix E Uncertainty Analysis

An uncertainty analysis was performed on the heat transfer calculations to determine the total uncertainty on the Nusselt numbers measured by each thin film gauge. The total uncertainty consists of a bias error and a precision error. The bias error is the error that is constant for a set of measurements. Typically, bias errors are the result of a calibration error. The bias error was determined using the perturbation method described by Moffat [F.15]. This method takes into account the error associated with the measurement and tracks the error as it propagates through calculations. The bias error for each experiment was calculated to be 8.5% with the majority of the error being associated to the uncertainties of the material properties of the Macor. Each gauge had the same bias error because the same gauges and data reduction technique was used on each one.

The precision error is the error that is due to the run to run repeatability of the measurements. The precision error was calculated using a statistical method provided in equation E-1,

$$P = \frac{t \cdot S_{Nu}}{\overline{Nu} \cdot \sqrt{N}} \tag{E-1}$$

where S_{Nu} is the standard deviation of the Nusselt number, Nu is the average Nusselt number , N is the number of runs and t is the value of a two sided Students-t distribution at a 90% confidence interval. The precision error varied for set of data and for each gauge. The minimum and maximum precision errors were calculated to be 0.2% and 7.8% respectively.

With the bias error and the precision error calculated, the total uncertainty could be calculated. The total uncertainty is given by equation E-2,

$$\Delta = \sqrt{B^2 + P^2} \tag{E-2}$$

where B is the bias error and P is the precision error. The average total uncertainty for all of the experiments is X%. A summary of the measurement errors for each set of heat transfer data is provided in Table E-1.

Table E-1. Summary of the experimental uncertainty for all of the experiments

Test Condition	Bias Error B, %	Precision Error P, %		Total Uncertainty, %	
		Min P, %	Max P, %	Min Δ, %	Max Δ, %
M = 0.60, Tu = 1.7 %	8.50	0.24	7.68	8.50	11.45
M = 0.60, Tu = 12.2 %	8.50	0.51	5.50	8.51	10.12
M = 0.60, Tu = 13.7 %	8.50	0.20	5.3	8.50	10.0
M = 0.80, Tu = 1.7%	8.50	0.26	5.09	8.50	9.91
M = 0.80, Tu = 12.2 %	8.50	1.55	6.71	8.64	10.83
M = 0.80, Tu = 13.7 %	8.50	0.34	6.50	8.51	10.71
M = 1.0, Tu = 1.7%	8.50	0.12	7.81	8.5	11.54
M = 1.0, Tu = 12.2 %	8.50	0.54	6.28	8.52	10.57
M = 1.0, Tu = 13.7 %	8.50	1.00	7.73	8.56	11.48

Appendix F References

[F.1] Jones and Launder, B. E., "The Prediction of Laminarization with a Two-Equation Model of Turbulence," *Intl. J. Heat and Mass Transfer*, **15**, 1972, pp. 301-314.

[F.2] Mayle, R.E., 1991, "The Role of Laminar-Turbulent Transition in Gas Turbine Engines," *ASME J. Turbomach.*, **113**, pp. 509-537.

[F.3] Giel, P. W., Boyle, R. J., and Bunker, R. S., 2004, "Measurements and Predictions of Heat Transfer on Rotor Blades in a Transonic Turbine Cascade," *ASME J. Turbomach.*, **126**, pp. 110-121.

[F.4] Nix, A.C., 2003 "Effects of High Intensity, Large-Scale Freestream Combustor Turbulence on Heat Transver in Transonic Turbine Blades," PhD Dissertation, Virginia Polytechnic Institute and State University.

[F.5] Baines, W.D. and Peterson, E.G., 1951, "An Investigation of Flow Through Screens," *Trans. of the ASME*, July 1951, pp. 467-480.

[F.6] Nix, A.C., Smith, A.C., Diller, T.E., Ng, W.F. and Thole, K.A., 2002, "High Intensity, Large Length-Scale Freestream Turbulence Generation in a Transonic Turbine Cascade," ASME GT-2002-30523.

[F.7] Sauer, J., 1996, "The SUDI Turbulence Generator – A Method to Generate High Freestream Turbulence Levels and a Range of Length Scales," Thesis, Univerisity of Wisconsin/ University of Karlsruhe, Germany.

[F.8] Hinze, J., 1975, *Turbulence*, 2nd Ed., McGraw-Hill, New York

[F.9] Roach, P.E., 1987, "The Generation of Nearly Isotropic Turbulence by Means of Grids," *Int. J. Heat Fluid Flow*, Vol. 8, No. 2, pp. 82-92.

[F.9] Roach, P.E., 1987, "The Generation of Nearly Isotropic Turbulence by Means of Grids," *Int. J. Heat Fluid Flow*, Vol. 8, No. 2, pp. 82-92.

[F.10] Schultz, D.L., and Jones, T.V., 1973, "Heat Transfer Measurements in Short Duration Hypersonic Facilities," AGARD AG-165.

[F.11] Joe, C.R., 1997, "Unsteady Heat Transfer on the Turbine Research Facility at Wright Laboratory," PhD Dissertation, Syracuse University

[F.12] Doorly, J.E., and Oldfield, M.L.G., 1987, "The Theory of Advanced Multi-Layer Thin Film Heat Transfer Gages," *Intl. J. Heat and Mass Transfer*, **30**, No. 6, pp. 1159–1168.

[F.13] Dunn., M.G., 1995, "The Thin-Film Gage," von Karman Institute for Fluid Dynamics, Lecture Series 1995-01.

[F.14] Cress, R.D., 2006, "Turbine Blade Heat Transfer Measurements in a Transonic Flow Using Thin Film Gages," Master's Thesis, Virginia Polytechnic Institute and State University.

[F.15] Moffat, R. J., 1988, "Describing Uncertainties in Experimental Results," *Exp. Thermal and Fluid Science*, 1988, pp. 3-17.